TRIUMF

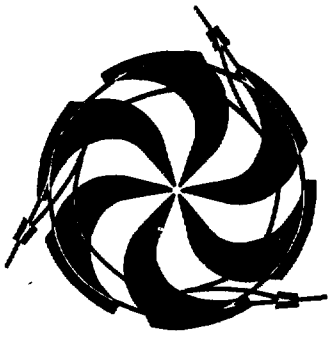

HIGH INTENSITY CIRCULAR PROTON ACCELERATORS

M.K. Craddock

Physics Department, University of British Columbia
and TRIUMF

CANADA's NATIONAL MESON FACILITY
OPERATED AS A JOINT VENTURE BY:

UNIVERSITY OF ALBERTA
SIMON FRASER UNIVERSITY
UNIVERSITY OF VICTORIA
UNIVERSITY OF BRITISH COLUMBIA

UNDER A CONTRIBUTION FROM THE
NATIONAL RESEARCH COUNCIL OF CANADA

TRI-87-2

TRI-87-2

HIGH INTENSITY CIRCULAR PROTON ACCELERATORS

M.K. Craddock

Physics Department, University of British Columbia
and TRIUMF

This report is based in part on material presented to the NATO Advanced Study Institute International Advanced Course on High-Brightness Accelerators held in Pitlochry, Scotland, July 13–25, 1986.

Postal address:

TRIUMF
4004 Wesbrook Mall
Vancouver, B.C.
Canada V6T 2A3

December 1987

Contents

HIGH INTENSITY CIRCULAR PROTON ACCELERATORS

Abstract

Circular machines suitable for the acceleration of high intensity proton beams include cyclotrons, FFAG accelerators, and strong-focusing synchrotrons. This paper discusses considerations affecting the design of such machines for high intensity, especially space charge effects and the role of beam brightness in multistage accelerators. Current plans for building a new generation of high intensity "kaon factories" are reviewed.

INTRODUCTION

The concept of beam brightness has come to play an important role in the design of multistage high intensity circular proton accelerators, through the space charge defocusing effects associated with high brightness. In this paper we first review the different types of circular proton accelerators and how focusing is provided; then discuss the effects of space charge forces, including the role of beam brightness in determining the number of accelerator stages required; and finally describe some current proposals for higher intensity machines.

Good general introductions to circular accelerators are given in the standard texts by Livingood (1961), Livingston and Blewett (1962) and Bruck (1966). Valuable review articles are also available on sector-focusing cyclotrons (Richardson, 1965), and high intensity accelerators (Courant, 1968). More recent developments are covered in the proceedings of the summer schools on high energy accelerators which have been held annually for the past few years in the U.S. (1981–) and in Europe; the schools held at Erice (CERN-ISPA, 1977) and in Paris (CERN, 1985) offer particularly good introductory articles. Finally, an excellent short survey of modern proton synchrotron design for beginners is given by E.J.N. Wilson (1977).

By "circular" accelerators we shall mean any machine in which the particles are bent into closed orbits, even though these may not be perfect circles but include segments that are straight or of different curvatures. This "recirculation" principle allows the beam to be passed repeatedly through the same electric accelerating fields, vastly reducing the complexity and cost of the accelerating equipment; the cost of the magnetic bending system is modest by comparison. The net result is a very high effective accelerating field gradient—as much as 150 MV/m for the Fermilab Tevatron, or 240 MV/m for the proposed SSC.

THE CYCLOTRON RESONANCE PRINCIPLE

For a proton of mass m and charge e moving with velocity $\mathbf{v}$ normal to magnetic induction $\mathbf{B}$, the Lorentz force $e\mathbf{v} \times \mathbf{B}$ provides the centripetal acceleration to bend the trajectory with radius of curvature ρ:

$$evB = \frac{mv^2}{\rho} \tag{1}$$

From this we can derive equations for the radius

$$\rho = \frac{mv}{eB} \tag{2}$$

which increases in proportion to momentum $p \equiv mv$, and for the angular frequency of rotation

$$\omega = \frac{eB}{m} . \tag{3}$$

Notice that whereas the radius ρ increases in proportion to momentum p for fixed B and m, the angular frequency and orbit time are constant, independent of velocity. Lawrence (1930) realized that this property of "*isochronism*" greatly simplified the problem of designing a circular accelerator, as a fixed frequency rf accelerating field would remain in synchronism with the ions as they were accelerated to greater momenta and radii (Fig. 1). Not only was the hardware design simplified but ions could be accelerated on every rf cycle in a quasi-continuous (cw) stream. The fruit of this "*cyclotron resonance principle*" was a successful series of fixed frequency cyclotrons of increasing size built by Lawrence and his students in the 1930s.

For protons of kinetic energy $T \simeq 20$MeV, however, a limit was reached. The relativistic increase in mass

$$\frac{m}{m_0} = \frac{E}{E_0} = 1 + \frac{T}{E_0} \equiv \gamma = \frac{1}{\sqrt{1-\beta^2}} \tag{4}$$

of about 2% disturbed the constancy of ω enough that over many turns the protons lost synchronism with the rf voltage peak and were no longer accelerated. (In the above notation $E_0 = m_0c^2$ denotes the "rest energy" and $\beta \equiv v/c$.)

WEAK FOCUSING

This problem was enhanced by the natural drop-off with radius of the magnetic field strength B between flat pole-faces—a drop-off that was found, however, to be essential to provide vertical focusing of the particles. (In accelerator usage "focusing" means containment of the particle beam within a not-too-large diameter, rather than formation of an image spot.) Figure 2 shows how a field decreasing with radius r is associated with a convex field pattern which provides restoring forces towards the median plane, while a field increasing with radius does the opposite. The horizontal and vertical focusing strengths are conventionally described in terms of the "tunes" ν_r and ν_z (Q_r and Q_z in Europe) —the numbers of "betatron" oscillations performed per turn about the stable orbit. The vertical component of the Lorentz force is given by

$$F_z = evB_r \simeq ev\frac{\partial B_r}{\partial z} z . \tag{5}$$

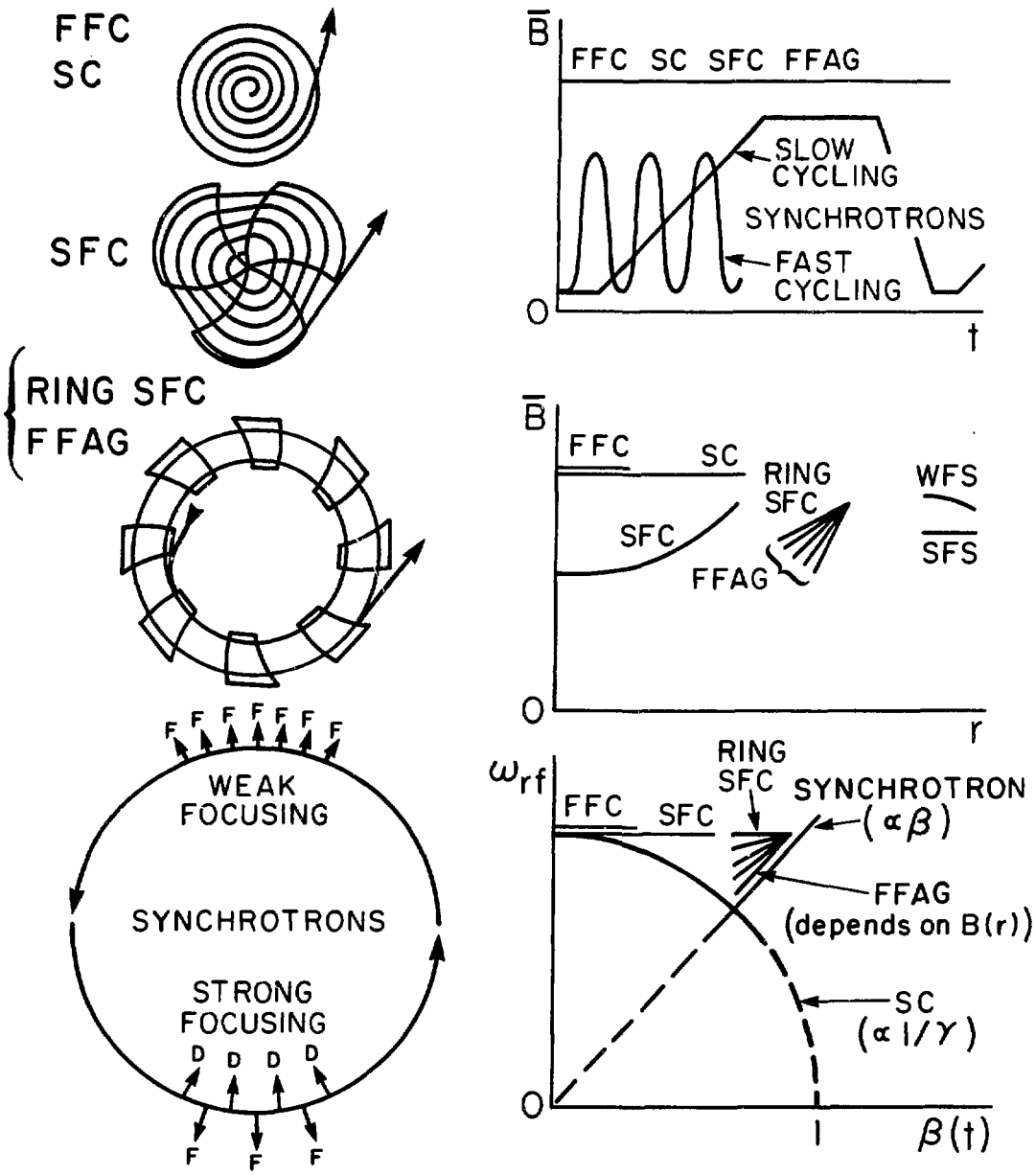

Figure 1: Beginner's guide to circular proton accelerators—schematic plans, magnetic field dependence on time and radius, and radiofrequency variation with velocity.

FFC	–	fixed frequency cyclotron	WFS	–	weak focusing synchrotron
SC	–	synchrocyclotron	SFS	–	strong focusing synchrotron
SFC	–	sector-focused cyclotron	FFAG	–	fixed field alternating gradient

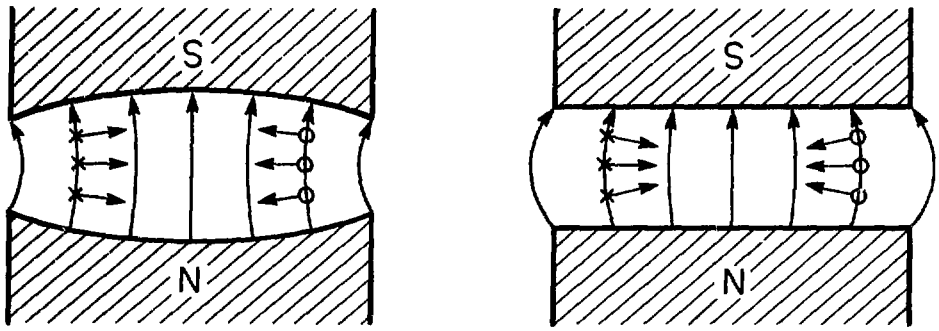

Figure 2: Vertical focusing (defocusing) effect of a radially decreasing (increasing) magnetic field. Protons travel in counterclockwise orbits seen from above.

But for stable betatron oscillations $F_z = -m\omega^2\nu_z^2 z$. Using Maxwell's equations and writing the logarithmic field gradient

$$k \equiv \frac{r}{B_z}\frac{\partial B_z}{\partial r} \tag{6}$$

the student will find (***Exercise 1***) that

$$\nu_z = \sqrt{-k}\,. \tag{7}$$

Similarly, for horizontal motion (***Exercise 2***)

$$\nu_r = \sqrt{1+k}\,. \tag{8}$$

Clearly k must be negative for vertical stability, but not too strongly so, or horizontal stability is lost. In this situation we require

$$-1 < k < 0 \tag{9}$$

but achieve only "weak" focusing

$$0 < \nu < 1\,. \tag{10}$$

SYNCHROCYCLOTRONS AND SYNCHROTRONS

Historically, the first technique used to overcome the energy limit posed by rising mass was modulation of the rf frequency in sympathy with the orbital frequency given by (3). For this to be practical for a real beam, spread out in time and momentum around the synchronous condition, there must be stable motion about this point in longitudinal phase space. The existence of longitudinal or "phase" focusing was proved independently by Veksler (1944) and McMillan (1945) and first demonstrated experimentally by Richardson *et al.* (1946).

In **synchrocyclotrons** the magnetic field is kept constant while the radiofrequency is modulated. The orbit radius increases with energy, just as in fixed frequency cyclotrons. The energy attainable is set by the cost of providing a large area of magnetic field; the

highest energy synchrocyclotron, at Gatchina in the USSR, has a pole diameter of 6.85 m, uses 7800 tons of steel and reaches 1000 MeV:

$$\begin{aligned} B &\simeq \text{constant} \\ \omega_{rf} &\propto 1/\gamma = \sqrt{1-\beta^2} \\ \rho &\propto \beta\gamma\,. \end{aligned} \tag{11}$$

In **synchrotrons** higher energies are brought within economic reach by keeping the orbit radius constant, thus shrinking the vacuum chamber from a hollow disc to a hollow ring and drastically reducing the area of magnetic field required for a given energy. To achieve this, the magnetic field strength must be modulated as well as the radiofrequency:

$$\begin{aligned} \rho &\simeq \text{constant} \\ B &\propto \beta\gamma \\ \omega &\propto \beta\,. \end{aligned} \tag{12}$$

The $B(t)$, $B(r)$ and $\omega_{rf}(\beta)$ dependence of these machines is illustrated in Fig. 1. In fast-cycling synchrotrons ($\gtrsim$ 3 Hz) the magnetic field is modulated harmonically; in slow cycling synchrotrons ($\lesssim$ 3 Hz) it follows a linear ramp, often with a short flat bottom for multi-turn injection and a long flat top for slow extraction. The latter is an essential feature for many counter-based experiments, which depend on coincidence techniques to identify the numerous reaction products and cannot tolerate a beam which is sharply pulsed.

This highlights one of the major characteristics of all frequency-modulated machines—they are operated in a *pulsed mode* where one group of particles has to go through a complete cycle of capture, acceleration and extraction before another can begin. As a result the beam intensities achievable are much lower ($\leq$ 1 μA on average) than for fixed frequency cyclotrons, which can be operated cw at milliampere currents.

Lower intensity is the price paid for reaching higher energies. In principle there is no upper limit to the particle energy which can be achieved in a synchrotron. In practice the limit is set by cost (mostly for the magnet). The largest weak focusing synchrotron using constant field gradient focusing is the 10 GeV "Synchrophasotron" at Dubna; 36000 tons of steel were used in the magnet, whose circumference is 175 m and beam aperture 1.50 m × 0.36 m. The enormous—and expensive—apertures of such machines are directly related to their large radii and weak focusing. To see this quantitatively, suppose the maximum amplitude betatron oscillation is described by

$$y = a\sin(\nu\theta + \delta)\,, \tag{13}$$

where y stands for transverse displacement, ν is the tune and θ the azimuthal angle. Then it is easy to show (***Exercise 3***) that if the maximum divergence angle is α, then

$$a = \alpha r/\nu\,, \tag{14}$$

so that small ν and big r lead to large a. To maintain constant a and α, ν must increase with r, as is obvious if one considers betatron oscillations of fixed wavelength in machines of different radii. Apparently stronger focusing is required to achieve higher energies.

SECTOR FOCUSING

An alternative source of vertical focusing had been proposed by Thomas (1938) in a scheme to allow higher energy cyclotrons to be built at fixed frequency. He proposed to maintain a constant orbit frequency (3) as the mass increased with energy and radius ($m = \gamma m_0$) by increasing the magnetic field strength commensurately (Fig. 1):

$$B = \gamma B_c = \frac{B_c}{\sqrt{1-(r/r_c)^2}} \,. \tag{15}$$

Here $B_c \equiv \omega m_0/e$ is the "central" field and $r_c \equiv c/\omega$ is the radius at which $v \to c$. Such a field profile of course gives a vertically defocusing field gradient (***Exercise 4***)

$$\nu_z^2 = -\beta^2\gamma^2 \,. \tag{16}$$

To counteract this Thomas proposed contouring the magnet pole faces to provide a sinusoidal azimuthal variation in field strength. In practice this can be achieved by dividing the poles into N symmetrical sectors, each consisting of a "hill" with small gap and high field B_h and a "valley" with large gap and low field B_v (Fig. 3). The different orbit curvatures in hill and valley lead to a scallopped closed orbit oscillating around a perfect circle. This implies a radial velocity component v_r, strongest at the hill-valley "edges" where the hill fringing field provides B_θ components away from the median plane. The result is a vertical Lorentz force component F_z which is focusing at every edge. This is in fact the *edge focusing* effect familiar in spectrometers and other magnets where a particle crosses a field change ΔB at an angle κ to the normal: the edge acts like a thin lens whose focal length f may be obtained (***Exercise 5***) by integrating along the orbit to obtain the total impulse and then using Stokes' theorem:

$$\frac{1}{f} = \frac{e\Delta B}{mv}\tan\kappa \,. \tag{17}$$

Some wrestling with the geometry of the scallopped orbit in this "hard edge field" approximation (***Exercise 6***) will convince the persevering reader that the "Thomas angle" κ is given by

$$\kappa = \frac{\pi}{N}\frac{(B_h-\overline{B})(\overline{B}-B_v)}{(B_h-B_v)\overline{B}} \,, \tag{18}$$

where $\overline{B}$ is the azimuthal average of B_h and B_v and has to obey (15). Normally κ is small enough to make small angle approximations valid. Exercise 13 below offers an opportunity to demonstrate that the lenses described by (17) make a net contribution to the vertical focusing equal to the field "flutter" F^2:

$$\Delta\nu_z^2 = F^2 \equiv \frac{\overline{(B-\overline{B})^2}}{\overline{B}^2} = \frac{(B_h-\overline{B})(\overline{B}-B_v)}{\overline{B}^2} \tag{19}$$

Sector focusing was first demonstrated experimentally in 1950-53 in model cyclotrons built by Richardson's group (Kelly *et al.*, 1956) for electrons up to $\beta \simeq 0.5$. The principle has led to the construction of a large number of high current "isochronous" fixed frequency cyclotrons. By removing all steel from the valley, making $B_v = 0$, and using only narrow hills, the "flutter" factor on the right-hand side of (18) may in principle be made as large

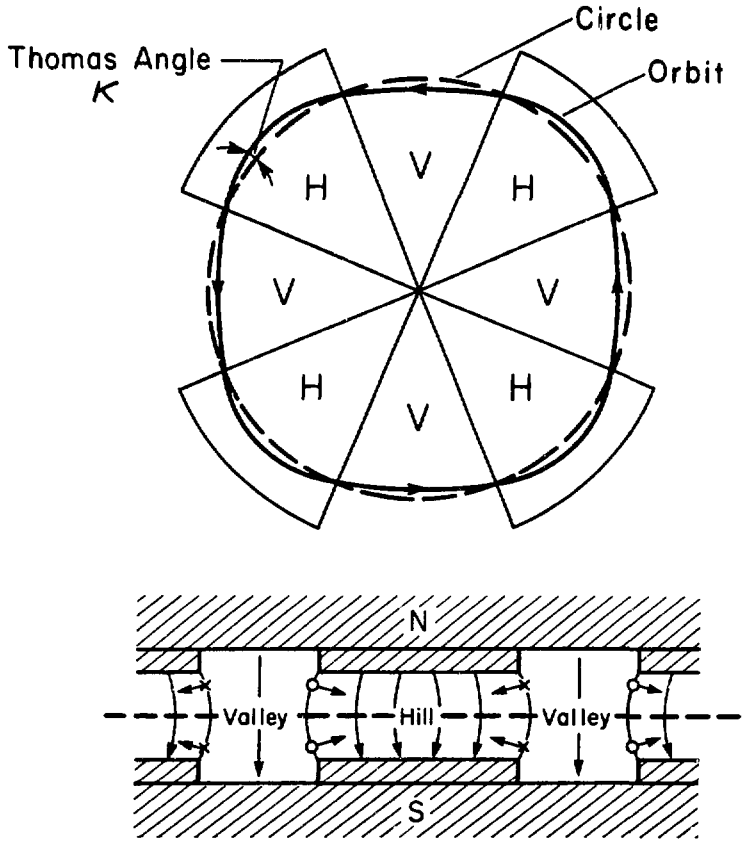

Figure 3: Vertical (Thomas) focusing effect of an azimuthally varying magnetic field created by radial magnet sectors; the radial velocity components associated with orbit scallopping provide vertical forces at the edge of each sector.

as desired. In practice the availability of strong spiral focusing (see below) has made the use of purely radial sector focusing uncommon for protons above 50 MeV.

Edge focusing was also used in the Argonne 12.5 GeV Zero Gradient Synchrotron, where the magnet was built in 8 separate sectors with angled ends. The strength of the vertical focusing, however, was no greater than in conventional weak focusing synchrotrons, since the drift spaces were rather short.

STRONG FOCUSING

It was the discovery of the strong focusing principle by Courant, Livingston and Snyder (1952), and independently by Christofilos, that provided the mechanism allowing both synchrotrons and cyclotrons to be built to even higher energies. They observed that a succession of focusing and defocusing lenses of equal strength have an overall focusing effect (provided their spacing is not large enough to allow cross-over). On average the displacement is greater at the F than at the D lenses (Fig. 4) and so the deflexions towards the axis are greater than those away from it. Since the F–D combination is focusing in both transverse

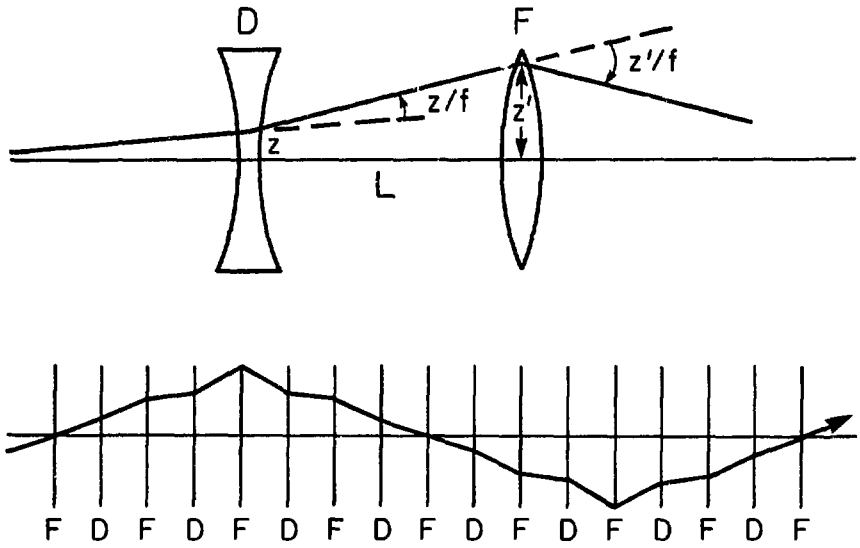

Figure 4: The strong focusing principle—net focusing effect of alternating focusing and defocusing lenses of equal focal length f. Note that the effect is the same in both directions, *i.e.* for FD and DF arrangements.

planes, much stronger lenses can be used than allowed by (9), and tune values $\nu \gg 1$ achieved. A formal treatment is given below.

For **synchrotrons** the use of magnets with alternating (focusing and defocusing) gradients made it economically feasible to build machines such as the Brookhaven AGS (33 GeV) and CERN PS (28 GeV) in which the tune values were raised to 6–9, the magnet apertures reduced to 6 cm × 3 cm, and the circumference increased to 600–800 m.

While these early designs used "combined function" gradient magnets which both bent and focused the beam, since about 1970 it has been usual to employ "separate function" magnets—quadrupoles for focusing and zero-gradient dipoles for bending.

With the help of stronger fields from superconducting magnets, proton synchrotron energies have recently been pushed towards 1000 GeV with the 7 km long Fermilab Tevatron. Future plans call for the construction of the 20 TeV Superconducting Super Collider (SSC); improvements in magnet design keep the circumference to 83 km, while the tune grows to 78.3 and the magnet aperture stays at 3 cm × 3 cm. These very high energy accelerators consist of a number of stages and we shall see below that the concept of beam brightness plays an important part in matching these stages together.

Fixed field alternating focusing accelerators have traditionally been known as FFAG (fixed field alternating gradient) accelerators, after the first electron models built at MURA, although later designs have tended to use edge rather than gradient focusing. In particular Kerst (Symon *et al.*, 1956) suggested setting the hill edges at large angles ε to a radius to form spiral ridges or sectors, obtaining much stronger edge focusing (Fig. 5).

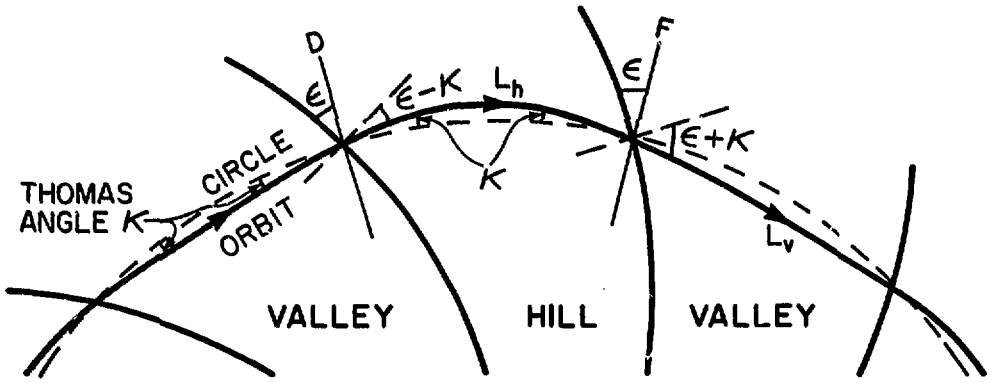

Figure 5: Geometry of scallopped orbits in a cyclotron with spiral sectors.

Alternate edges would be focusing and defocusing, with focal powers given by

$$\frac{1}{f} = \pm\frac{e\Delta B}{mv}\tan(\varepsilon \pm \kappa) \qquad (17')$$

but the net effect would of course be strongly focusing.

FFAG accelerators, with fixed magnetic field but modulated rf, are the strong focusing analogues of synchrocyclotrons; however, they are generally designed with a rising rather than flat field profile $B(r)$, in order to narrow the range of orbit radii, and hence the magnet aperture, giving a less costly ring-shaped machine (Fig. 1). No FM proton FFAGs have ever been built, although there have recently been proposals for 1–3 GeV versions as spallation neutron sources (Khoe and Kustom, 1983; Meads and Wüstefeld, 1985).

Fixed frequency alternating focusing accelerators are however ubiquitous, in the form of **isochronous cyclotrons** with spiral sectors. These may be regarded as an extreme form of FFAG accelerator in which $B(r)$ follows (15) to keep the orbital frequency constant, and the rf frequency modulation is consequently reduced to zero. The additional vertical focusing provided by the spiral edges allows the defocusing (16) associated with isochronism to be compensated to much higher energies, while cw operation permits high currents to be accelerated. Thus proton beams exceeding 200 μA have been extracted from the 500 MeV TRIUMF cyclotron (Zach, Dutto *et al.*, 1985) and the 590 MeV SIN cyclotron. With a new injector cyclotron (Joho *et al.*, 1985) SIN expects to raise the beam current above 1 mA. TRIUMF has studied spiral ring cyclotron designs using superconducting magnets that would accelerate protons above 10 GeV (Botman *et al.*, 1983).

TRANSVERSE MOTION IN PERIODIC LATTICES

Suppose a curvilinear co-ordinate system is taken, based on the equilibrium closed orbit, with s tangential, x normal horizontal outwards, and z vertical upwards (Fig. 6). The equations of motion for transverse (betatron) oscillations in either x- or z-plane then take the form of the Hill equation

$$\frac{d^2y}{ds^2} + k(s)y = 0 \qquad (20)$$

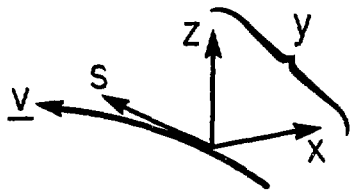

Figure 6: Orbit co-ordinate system.

where y stands for x or z, second and higher order terms have been omitted, and momentum-dependent effects are ignored. The function $k(s)$ describes the variation in focusing strength along the orbit. In any accelerator $k(s)$ will be periodic over the complete circumference C; in addition in strong focusing synchrotrons and cyclotrons where the machine is composed of a number (N) of identical superperiods, cells or sectors, $k(s)$ will be periodic over their length (L). The solutions to (20) may be shown to be of the quasi-periodic form

$$y(s) = \sqrt{\varepsilon\beta(s)}\cos[\psi(s) + \delta]\,. \tag{21}$$

Here the cosine term represents the betatron oscillation, whose phase is determined partly by the "phase function" $\psi(s)$, which varies around the orbit, and partly by the arbitrary angle δ. The amplitude of the oscillation is given by $\sqrt{\varepsilon\beta(s)}$ —the product of a position-independent factor ε and the "amplitude function" or "beta function" $\beta(s)$, which varies with position within a cell, but is the same for each identical cell.

Differentiating (21) we obtain an expression for the divergence angle

$$y'(s) \equiv \frac{dy}{ds} = -\sqrt{\varepsilon\beta}\frac{d\psi}{ds}\sin(\psi + \delta) + \frac{1}{2}\sqrt{\frac{\varepsilon}{\beta}}\frac{d\beta}{ds}\cos(\psi + \delta)\,. \tag{22}$$

Equations (21) and (22) will be recognized as the parametric equations for a tilted ellipse in y–y' phase space (Fig. 7). As a particle moves around the machine $\beta(s)$ will change, altering the shape of the ellipse, and so will $\psi(s)$, moving the representative point around the ellipse once for each betatron oscillation and ν times for each orbit. At a given point of the orbit, different values of δ (ranging from 0 to 2π) describe different locations around the ellipse, while different values of ε represent ellipses of different sizes (but the same shape). A beam of particles with all phases of oscillation, and all amplitudes up to some maximum, can therefore be described by a set of representative points entirely filling an ellipse in phase space defined by the largest ε and the local $\beta(s)$.

Eliminating the phase angles $(\psi + \delta)$ between (21) and (22) (***Exercise 7***) gives the Cartesian equation of the ellipse

$$\gamma(s)y^2 + 2\alpha(s)yy' + \beta(s)(y')^2 = \varepsilon \tag{23}$$

where the "Twiss parameters" are defined by

$$\alpha(s) \equiv -\frac{1}{2}\frac{d\beta}{ds} \tag{24}$$

$$\gamma(s) \equiv \frac{1+\alpha^2}{\beta(s)}\,. \tag{25}$$

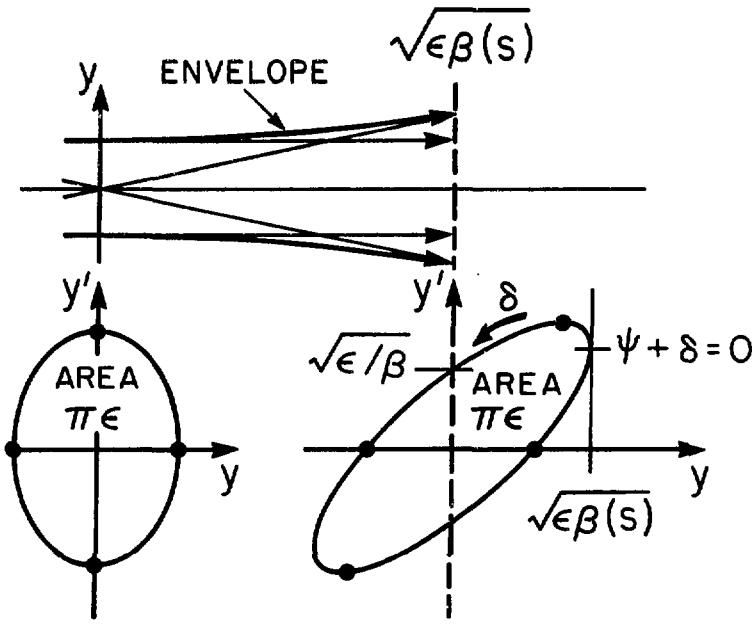

Figure 7: Elliptical envelopes of a beam in the y–y' phase plane: left, waist; right, in a divergent region.

The parameter $\alpha(s)$ describes the tilt of the ellipse ($\alpha = 0$ for one that is upright), while $\gamma(s)$ defines the maximum divergence $y'_{\max} = \sqrt{\varepsilon\gamma}$ (just as $\beta(s)$ defines the maximum displacement $y_{\max} = \sqrt{\varepsilon\beta}$).

The area of the ellipse given by (23) represents the "emittance" of a beam of particles whose representative points are enclosed by it:

$$E = \pi\varepsilon \,. \tag{26}$$

Thus the phase space area is constant, as required by Liouville's theorem for all processes describable by a Hamiltonian function, such as charged particle motion in electric and magnetic fields. But in deriving (23) it is only possible to make the area constant, independent of s, by requiring

$$\frac{d\psi}{ds} = \frac{1}{\beta(s)} \,. \tag{27}$$

Thus there is only one independent function of s —usually taken to be $\beta(s)$. Not only $\alpha(s)$ and $\gamma(s)$, but also the phase angle $\psi(s)$, can be derived from it:

$$\psi(s) = \int \frac{ds}{\beta(s)} \,. \tag{28}$$

Integrating (28) around a complete orbit of circumference $2\pi R$ we see that the average

$$\left\langle \frac{1}{\beta(s)} \right\rangle = \frac{\nu}{R} = \frac{2\pi}{\lambda} \tag{29}$$

where λ represents the wavelength of a betatron oscillation.

A differential equation for the function $\beta(s)$ may be obtained (***Exercise 8***) by substituting (21) into (20):

$$\frac{1}{2}\beta\frac{d^2\beta}{ds^2} - \frac{1}{4}\left(\frac{d\beta}{ds}\right)^2 + k(s)\beta^2 = 1\,. \tag{30}$$

This may readily be converted into a differential equation for the "envelope function" $y_m(s) = \sqrt{\varepsilon\beta}$ —just (20) modified by a cubic term:

$$\frac{d^2y_m}{ds^2} + k(s)y_m - \frac{\varepsilon^2}{y_m^3} = 0\,. \tag{31}$$

Figure 8 illustrates the envelope function and several individual orbits for a FODO lattice of regularly spaced quadrupoles. Notice that the envelope is periodic over the cell length while the betatron oscillations have a much longer wavelength.

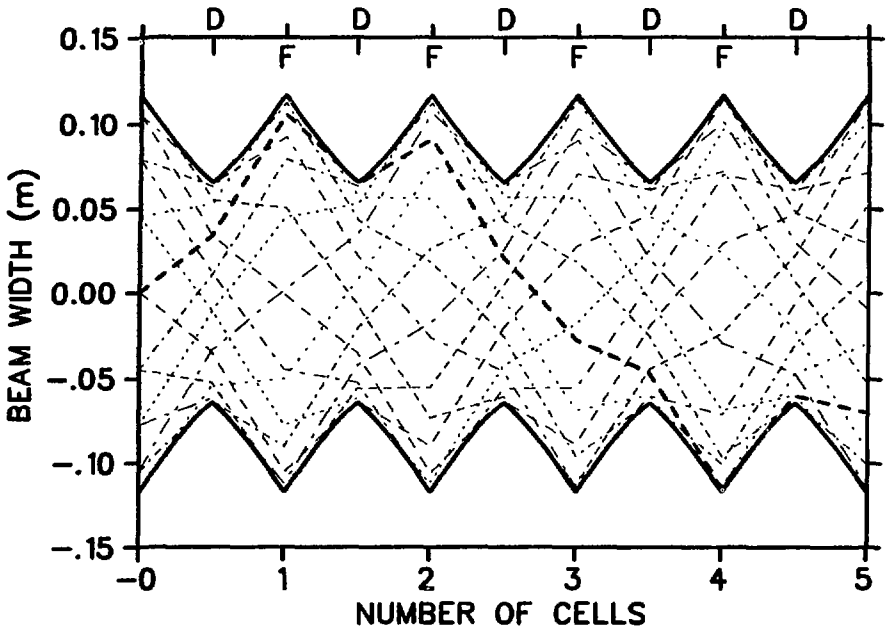

Figure 8: Selected orbits and their envelope function for a regular FODO thin lens lattice.

EVALUATION OF THE FOCUSING STRENGTH

It is a property of the Hill equation (20) that solutions $y(s)$ at point s can be expressed in terms of the displacement $y_0 \equiv y(s_0)$ and divergence $y_0' \equiv y'(s_0)$ at some point s upstream by means of a linear superposition of "cosine-like" and "sine-like" solutions $C(s)$ and $S(s)$, where $C(s_0) = 1$ and $S(s_0) = 0$:

$$y(s) = C(s)y_0 + S(s)y_0'\,. \tag{32}$$

Consequently it is possible to express the relation between the co-ordinates at s and s_0 by a matrix equation

$$\begin{bmatrix} y(s) \\ y'(s) \end{bmatrix} = \begin{bmatrix} M_{11} & M_{12} \\ M_{21} & M_{22} \end{bmatrix} \begin{bmatrix} y_0 \\ y'_0 \end{bmatrix} \tag{33}$$

where the elements of the "transfer matrix" M depend on both s and s_0. Now suppose that the matrix M describes one complete cell of the lattice, so that

$$s = s_0 + L$$

and

$$\psi(s) = \psi(s_0) + \mu \tag{34}$$

where μ denotes the "phase advance". Then the Twiss parameters, α, β, γ take the same values at s and s_0, and if we use (34) to expand the expressions (21) for $y(s)$ and (22) for $y'(s)$ in terms of y_0 and y'_0 we find (***Exercise 9***)

$$M = \begin{bmatrix} \cos\mu + \alpha\sin\mu & \beta\sin\mu \\ -\gamma\sin\mu & \cos\mu - \alpha\sin\mu \end{bmatrix}. \tag{35}$$

If M can be constructed independently of (35) by multiplying together known matrices for each element of the cell, then the resultant matrix elements M_{ij} will yield solutions for α, β and γ at the ends of the cell, and for

$$\cos\frac{2\pi\nu}{N} = \cos\mu = \frac{1}{2}(M_{11} + M_{22}), \tag{36}$$

yielding the value of the betatron tune ν.

For a **separated function synchrotron** we suppose that the quadrupole magnets are arranged in a regularly-spaced FODO lattice (Fig. 8) and that they can be treated as thin lenses. Any focusing action by the bending magnets will be neglected; (even with zero field gradient, there may be small edge focusing or weak focusing effects (cf. (8) above). Then a complete cell can be thought of as consisting of four elements—a focusing lens of focal length f, a drift space $L/2$, a defocusing lens of focal length $-f$ and a second drift space $L/2$. [For a quadrupole of length l and field gradient g, $f \simeq (B\rho)/lg$.] The transfer matrix for the whole cell can be formed by multiplying together the matrix operators for each element in sequence:

$$\begin{aligned} M &= M_0 M_D M_0 M_F \\ &= \begin{bmatrix} 1 & L/2 \\ 0 & 1 \end{bmatrix} \begin{bmatrix} 1 & 0 \\ 1/f & 1 \end{bmatrix} \begin{bmatrix} 1 & L/2 \\ 0 & 1 \end{bmatrix} \begin{bmatrix} 1 & 0 \\ -1/f & 1 \end{bmatrix}. \end{aligned} \tag{37}$$

Readers not familiar with matrix optics should check (***Exercise 10***) that the forms given for M_0, M_F and M_D do have the expected effects on parallel and divergent incident rays (represented by vectors $\begin{bmatrix} 1 \\ 0 \end{bmatrix}$ and $\begin{bmatrix} 0 \\ 1 \end{bmatrix}$).

Multiplying out the matrix M and comparing it with (35) above (***Exercise 11***) yields the following expressions for the phase advance μ and the β-value at the F quadrupole (or at the D quadrupole by changing the sign of f)

$$\sin\frac{\mu}{2} = \frac{L}{4f} \tag{38}$$

$$\beta_{\pm} = \frac{L}{\sin\mu}(1 \pm \sin\frac{\mu}{2}) . \tag{39}$$

The maximum and minimum β-values β_+ and β_-, occurring at the F and D quadrupoles respectively, are plotted in Fig. 9 as a function of μ. There is a rather flat minimum in β_+ for $\mu \simeq 78°$; for economy in magnet apertures μ is usually chosen in this region, leading to tune values $\nu \simeq N/4$.

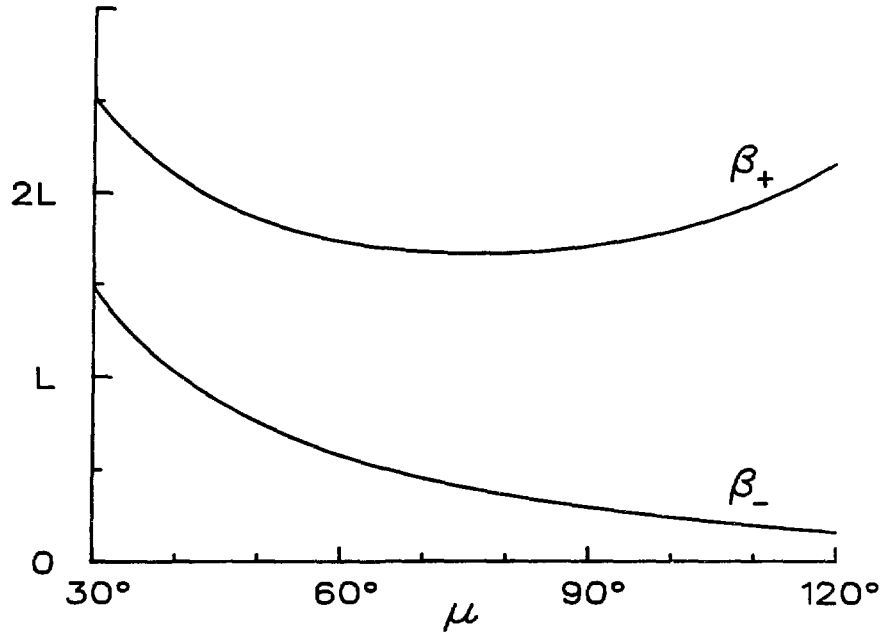

Figure 9: Variation of maximum and minimum β-values (β_+ and β_- at F and D quadrupoles respectively) with phase advance μ for a regular FODO thin lens lattice.

The usual scaling law with machine radius R is to increase the number of cells $N \propto \sqrt{R}$ (Reich, Schindl & Schönauer, 1983). The reader may confirm (***Exercise 12***) that this choice results in several other quantities (tune ν, cell length L, beta function β and quadrupole strength ($\propto p/f$)) having to grow only at the same modest rate $\propto \sqrt{R}$. Thus the SSC and the Brookhaven AGS, whose circumferences are in the ratio 83km/0.81km = 103, have ratios of $444/60 = 7.4$ in N and $78.3/8.75 = 9.0$ in ν, close to $\sqrt{103} = 10.1$.

For a **sector focusing cyclotron** we will consider just vertical focusing, which is the most crucial because of the defocusing associated with isochronism (Eq. 16) and the proximity of the magnet poles. We suppose that the hills are much wider than the pole gap so that the hill and valley fields B_h and B_v are uniform and hard-edged. Each sector thus consists of two edge-focusing/defocusing thin lenses separated by drift spaces of length L_h and L_v (Fig. 5). The lenses have focal powers $1/f = \pm G\tan(\varepsilon \pm \kappa)$ (see Eq. (17′)) where G can be expressed in terms of the radii of curvature, ρ_h, ρ_v:

$$G \equiv \frac{e\Delta B}{mv} = \frac{B_h - B_v}{\bar{B}R} = \frac{1}{\rho_h} - \frac{1}{\rho_v} \tag{40}$$

If the spiral angle $\varepsilon > \kappa$, the Thomas angle, we have a FODO cell, but a more complicated one than evaluated for the synchrotron above, since the lenses are of different strengths and the drift spaces of different lengths. (For very small spiral angles, $\varepsilon < \kappa$, the cell is reduced to FOFO form.) The transfer matrix is given by

$$\begin{aligned} M &= M_0' M_D M_0 M_F \\ &= \begin{bmatrix} 1 & L_v \\ 0 & 1 \end{bmatrix} \begin{bmatrix} 1 & 0 \\ G\tan(\varepsilon-\kappa) & 1 \end{bmatrix} \begin{bmatrix} 1 & L_h \\ 0 & 1 \end{bmatrix} \begin{bmatrix} 1 & 0 \\ -G\tan(\varepsilon+\kappa) & 1 \end{bmatrix}. \end{aligned} \tag{41}$$

Multiplying this out and comparing it to (35) (***Exercise 13***) we can obtain expressions for the phase advance μ per cell and the β-values at the focusing and (changing the sign of ε) defocusing edges

$$\sin\frac{\mu}{2} = \frac{1}{2}\sqrt{2GL\kappa(1+\tan^2\varepsilon) + G^2 L_h L_v \tan^2\varepsilon} \tag{42}$$

$$\beta_\pm = \frac{L}{\sin\mu}\left[1 \pm 2\kappa\tan\varepsilon - \kappa^2(2+3\tan^2\varepsilon)\right] \tag{43}$$

where small angle approximations have been used for κ. Note that the smallness of the Thomas angle also limits the oscillations in the β-function, which are generally not as marked as in synchrotrons. The phase advance is also usually small enough to allow use of the small angle approximation for $\mu/2$ in (42), so that, using (18) and (40), and including the isochronous defocusing term (16), the reader will find the following expression for the overall vertical tune

$$\nu_z^2 = -\beta^2\gamma^2 + F^2(1+2\tan^2\varepsilon)\,. \tag{44}$$

Spiralling the sectors clearly provides a strong alternating focusing enhancement to the weak Thomas flutter focusing. For zero spiral angle Eq. (44) agrees with Eq. (19) quoted above.

TRANSVERSE SPACE CHARGE DEFOCUSING

High beam intensity and brightness affect many aspects of accelerator design and operation, but particularly beam dynamics (defocusing and instabilities), the rf accelerating system (beam loading), shielding and safety. The principal beam dynamic effect is transverse defocusing, due to mutual repulsion of the electrically charged particles making up the beam.

To evaluate this, we assume for simplicity that the beam is of circular cross-section (area A) with uniform charge density ρ, and that these quantities do not vary around the orbit (radius R, charge Ne), so that $\rho = Ne/2\pi RA$. Also we use polar co-ordinates (r,ϕ) centred on the beam axis (Fig. 10), with $r \ll R$. Then the self-fields produced by the electric charge and associated current can be written

$$E_r = \frac{\rho}{2\varepsilon_0} r \tag{45}$$

$$B_\phi = \frac{\rho}{2\varepsilon_0}\frac{v}{c^2} r \tag{46}$$

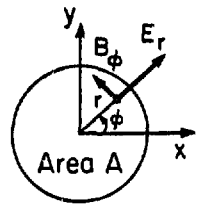

Figure 10: Cross-section and self-fields of an axially symmetric beam.

where $v = \beta c$ is the particle velocity. These fields exert a Lorentz force $e(\mathbf{E} + \mathbf{v} \times \mathbf{B})$ on individual protons, where the two terms tend to cancel as $v \to c$; the net force is easily seen to be of the entirely radial form

$$\Delta F_r = \frac{e}{2\varepsilon_0}\frac{\rho}{\gamma^2} r \,. \tag{47}$$

(Confirmation of this and the following derivations constitutes ***Exercise 14.***) Note that the defocusing force is linear in r just like the basic focusing force F_r which determines the tune ν:

$$F_r = -m(\omega\nu)^2 r = -\frac{m_0 c^2}{R^2}(\beta^2\gamma)\nu^2 r \,. \tag{48}$$

The net effect of ΔF_r is thus to decrease the tune by an amount $\Delta\nu$, the "tune shift," given by

$$2\nu\Delta\nu \simeq \Delta\nu^2 = -\frac{r_p R}{A}\frac{N}{\beta^2\gamma^3} \tag{49}$$

where a number of constants have been collected together in $r_p = e^2/4\pi\varepsilon_0 m_0 c^2 = 1.5347 \times 10^{-18}$ m, the classical radius of the proton. Besides its not-unexpected dependence on N and A, the tune shift depends very strongly on energy, but inversely, so that $\Delta\nu$ is greatest at the lowest energy—at injection. Since there is an upper limit to $\Delta\nu$ if serious betatron resonances are not to be crossed, this defines the lowest injection energy which can be used for a given R, N and A. Note, however, that the full $\beta^2\gamma^3$ dependence only applies for beams of *fixed area* A, independent of energy, such as those defined by a magnet aperture. Thus increasing the Brookhaven linac injector energy from 50 MeV to 200 MeV potentially increases the charge accelerable in the AGS for a fixed tune shift by the $\beta^2\gamma^3$ factor of 5.0, but to achieve it the magnet aperture must be filled to the same extent at the two injection energies.

A given beam, however, will shrink in transverse dimensions as it is accelerated. This "adiabatic shrinking" is essentially due to the longitudinal momentum of the particles $p_s \simeq p$ being increased while their transverse momentum components remain unchanged. Liouville's theorem requires the area occupied by the beam in y–p_y phase space to be conserved. Areas in y–y' space, which we have been considering, will change with forward momentum p. To recover the invariant property we multiply the emittance by a factor proportional to momentum to obtain the "*normalized emittance*"

$$\varepsilon^* = \beta\gamma\varepsilon \,. \tag{50}$$

Since the aperture and tune define ε independent of energy, the normalized emittance of the beam injected at 200 MeV in the example above will be larger by the momentum

factor 2.1 than that injected at 50 MeV, and its physical diameter will be larger by a factor $\sqrt{2.1}$ at any given energy.

If, on the other hand, we consider a given beam with a *fixed normalized emittance* ε^* then its cross-sectional area will decrease inversely as $\beta\gamma$:

$$A = \pi\varepsilon\beta_y = \pi\frac{\varepsilon^*}{\beta\gamma}\frac{R}{\nu} \tag{51}$$

where we have used (29) for the transverse beta-function β_y. In this case (49) becomes

$$\Delta\nu = -\frac{r_p}{2\pi}\frac{N}{\varepsilon^*}\frac{1}{\beta\gamma^2} \tag{52}$$

showing a reduced $\beta\gamma^2$ energy dependence. This shows how the tune shift varies as a given beam is accelerated, or how the accelerable charge Ne increases with injection energy for a given emittance and tune shift (a factor 2.4 for the Brookhaven example if no effort is made to maintain A by transverse stacking).

Equation (52) is also notable in showing that the tune shift is directly proportional to the normalized one-dimensional *beam brightness*

$$B_1^* = \frac{e\omega}{2\pi}\frac{N}{\varepsilon^*} \tag{53}$$

Equation (52) has been derived for the simplest conditions—a continuous "coasting" beam of uniform charge density and circular cross-section which has no interaction with its environment. For more complicated conditions the same basic dependences remain valid but additional factors are required (Reich *et al.*, 1983):

$$\Delta\nu = -\frac{r_p}{\pi}\frac{N}{\varepsilon^*}\frac{1}{\beta\gamma^2}\frac{FGH}{B_f}\,. \tag{54}$$

The "bunching factor" $B_f \equiv \overline{I}/I_{\max}$ describes the extent to which the beam is bunched longitudinally by the rf accelerating field. For a given average current $\overline{I}$, the greater charge density in a bunched beam increases $\Delta\nu$ proportionately.

The factor F describes the effect of image forces from the vacuum chamber and magnet poles. It was first derived by Laslett (1963) and indeed the whole expression (54) is often referred to as the Laslett incoherent tune shift. F has a complicated dependence on the energy, the bunching factor and the heights and widths of the beam, the vacuum chamber and the magnet poles. At low energies the image terms are negligible and $F \simeq 1$. For $\Delta\nu_z$ the electric image terms become important for $\gamma > h/b\sqrt{B_f}$ and the magnetic image terms for $\gamma > g/b\sqrt{B_f}$ where h, g and b are the half-heights of the vacuum chamber, magnet poles and beam respectively (Fig. 11).

The factor G describes the transverse density distribution. $G = 1$ for a uniform and 2 for a parabolic distribution; in practice G usually lies between 1 and 2. The factor H takes into account the aspect ratio (width/height = a/b) of non-circular beams. Locally $H_z = 1/(1 + a/b)$ and averaging over the orbit $\overline{H}_z = 1/(1 + \sqrt{\varepsilon_x\nu_z/\varepsilon_z\nu_x})$. Thus widening the beam can be effective in reducing H_z below the "circular" value 1/2, at the expense of increasing $\overline{H}_x$.

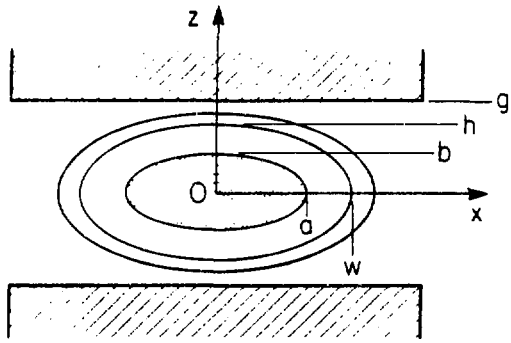

Figure 11: Cross-section of the beam aperture, showing magnet poles, vacuum chamber and beam.

While (54) is valid for all types of circular accelerator, for the same average current its effects are of course much more pronounced for pulsed machines (synchrocyclotrons, synchrotrons, FFAG) than for cw ones (isochronous cyclotrons). For slow cycling synchrotrons the duty factor is of order 10^{-6}, giving a million-fold enhancement and often making tune shift the crucial intensity-limiting factor. Synchrotrons designed for the highest intensities therefore tend to be fast-cycling, with lower charges Ne per pulse.

OFF-MOMENTUM ORBITS

As the momentum varies, so will the average radius R, the period and angular frequency of an orbit. For cyclotrons and FFAG machines with fixed magnetic field there exists an equilibrium (closed) orbit for each momentum, with a radius which generally increases with momentum. For synchrotrons, where the magnetic field is raised in proportion to the momentum, a central orbit (C.O.) is defined by the geometry (e.g. by the axes of the quadrupole magnets). At any given field level this central orbit is closed for one particular momentum value p. For a slightly different momentum $p_0 + \delta p$ there will be a slightly different closed orbit, deviating from the C.O. by

$$x(s) = \eta_x(s)\delta p/p_0 \tag{55}$$

where this equation defines the horizontal dispersion function $\eta_x(s)$. For weak focusing synchrotrons it is easy to show (***Exercise 15***) that

$$\eta_x(s) = \frac{R}{1+k} = \frac{R}{\nu_x^2} \tag{56}$$

so that with $\nu_x^2 < 1$ the dispersion is quite large and uniform around the machine.

For a strong focusing synchrotron with a regular FODO lattice $\eta_x(s)$ will be periodic over each cell, oscillating in phase with $\beta_x(s)$; by symmetry its slope will be zero at both focusing and defocusing quadrupoles

$$\eta'_+ = \eta'_- = 0\,. \tag{57}$$

Adding a third component to our matrix representation to describe the momentum deviation we may write

$$\begin{bmatrix} \eta_- \\ 0 \\ 1 \end{bmatrix} = M \begin{bmatrix} \eta_+ \\ 0 \\ 1 \end{bmatrix} \tag{58}$$

where the matrix M describes the effect of the half-cell between the centres of an F and a D quadrupole:

$$\begin{aligned} M &= M_{D/2} M_{\theta/2} M_{F/2} \\ &= \begin{bmatrix} 1 & 0 & 0 \\ 1/2f & 1 & 0 \\ 0 & 0 & 1 \end{bmatrix} \begin{bmatrix} 1 & L/2 & L\theta/8 \\ 0 & 1 & \theta/2 \\ 0 & 0 & 1 \end{bmatrix} \begin{bmatrix} 1 & 0 & 0 \\ -1/2f & 1 & 0 \\ 0 & 0 & 1 \end{bmatrix} \end{aligned} \tag{59}$$

where the angle of bend $\theta/2$ is assumed small enough for the small angle approximation to hold. (A comparison with (37) above will show the equivalence of the 2×2 x-x' sub-matrices to those used previously.) Evaluating (59) (***Exercise 16***) shows that

$$\eta_\pm = R\left(\frac{\pi/N}{\sin\mu/2}\right)^2 (1 \pm \tfrac{1}{2}\sin\mu/2) \tag{60}$$

so that on average

$$\overline{\eta_x} \simeq \frac{R}{\nu_x^2} . \tag{61}$$

This is the same as (56) for a weak focusing synchrotron, although the stronger tune here drastically reduces the magnitude of the dispersion. It should be noted, however, that relation (61) can break down for more complicated lattices, such as those with superperiodicity.

What of the momentum-induced changes in orbital period τ and angular frequency ω? Here we have the differential relations

$$\frac{\delta\omega}{\omega} = -\frac{\delta\tau}{\tau} = \frac{\delta v}{v} - \frac{\delta R}{R} . \tag{62}$$

At low energy it is possible for the increase in velocity to be greater than that in radius, and a higher momentum particle will orbit faster. At higher energies, however, as $v \to c$, the increase in radius will dominate and extra momentum will produce a slower orbit. Eq. (62) can be rewritten (***Exercise 17***) in terms of the parameter η (not to be confused with η_x)

$$\eta \equiv \frac{\delta\omega/\omega}{\delta p/p} = \frac{1}{\gamma^2} - \frac{\overline{\eta_x}}{R} . \tag{63}$$

This parameter plays a crucial role in the theory of longitudinal motion in synchrotrons. At low enough energies η is positive, but it decreases as the energy rises (Fig. 12), approaching $-\overline{\eta_x}/R$ asymptotically. (Readers are warned that η is sometimes defined with the opposite sign.) The critical energy at which η changes sign and a high momentum orbit changes from being faster to slower is known as the *transition energy* γ_t:

$$\gamma_t = \sqrt{\frac{R}{\overline{\eta_x}}} \simeq \nu_x . \tag{64}$$

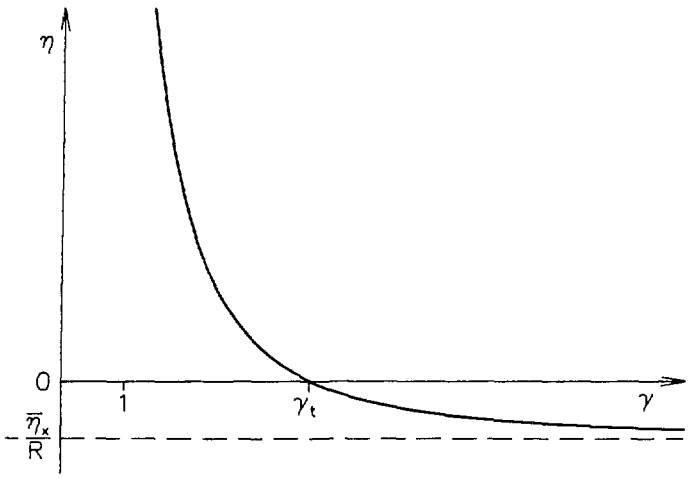

Figure 12: Dependence of η on energy.

Weak focusing machines have $\nu_x < 1$ and therefore always operate above transition. In strong focusing machines with regular lattices the horizontal tune is usually such that γ_t lies within the acceleration range. At this energy the machine becomes isochronous for all momenta and phase focusing disappears, as we shall see below, creating a potential trouble spot.

ACCELERATION AND PHASE STABILITY

At each instant t the magnetic field strength $B(t)$ defines the momentum $p_0(t)$ for the central orbit, and the corresponding orbital frequency $\omega_0(t)$. The rf voltage at an accelerating gap should therefore oscillate at an integer multiple frequency $h\omega_0$ given by the "harmonic number" h:

$$V = V_0 \sin h\omega_0 t \tag{65}$$

In discussing the longitudinal motion the rf phase angle $\phi = h\omega_0 t$ at the moment of an ion's crossing the accelerating gap is the conventional choice for co-ordinate. (Note that at a given instant ϕ is also a measure of the longitudinal position of different ions.) As time progresses the field B will rise, and with it the C.O. momentum p_0. Assuming V_0 is big enough there will be some "synchronous phase" ϕ_s for which the energy gain $eV_0 \sin \phi_s$ provides just the right momentum gain to keep the "synchronous particle" on the C.O. and at that same phase on later turns (***Exercise 18***):

$$V_0 \sin \phi_s = 2\pi R^2 \frac{dB}{dt} . \tag{66}$$

(Here we have assumed that the orbit encloses zero magnetic flux, so that there is no inductive (betatron) acceleration.) In practice B is increased either sinusoidally or linearly, depending on whether the cycling rate is fast or slow; in the latter case $V_0 \sin \phi_s$ = constant.

Since the rf voltage oscillates h times during one orbit period, there will be h places around the orbit where a synchronous particle can be found. As we shall now see, neigh-

bouring particles undergo stable oscillations about these places, if their amplitudes are not too large, defining stable "buckets" in longitudinal phase space.

To understand the motion of these not-quite-synchronous particles we must investigate the rates of change of their energy and phase (***Exercise 19***). Comparing a particle at phase ϕ, for which the energy gain per turn is

$$\frac{2\pi}{\omega}\frac{dE}{dt} = eV_0 \sin\phi\,, \tag{67}$$

with the synchronous particle, it may be shown that the energy difference ΔE between the two obeys

$$\frac{d}{dt}\left(\frac{\Delta E}{\omega_0}\right) = \frac{eV_0}{2\pi}(\sin\phi - \sin\phi_s)\,. \tag{68}$$

(ΔE, Δp, $\Delta\omega$ etc., will all denote differences from the synchronous values.) The rate of change of phase may be derived from (63):

$$\frac{d\phi}{dt} = \frac{-h\eta}{m_0 R_0^2}\left(\frac{\Delta E}{\omega_0}\right)\,. \tag{69}$$

Noting that the "momentum" co-ordinate canonically conjugate to the "position" co-ordinate ϕ is

$$W \equiv \frac{\Delta E}{\omega_0} = R_0 \Delta p \tag{70}$$

we see (***Exercise 20***) that (68) and (69) have the form of Hamilton's equations of motion for a system defined by the Hamiltonian function

$$H(\phi, W) = \frac{h\eta}{2m_0 R_0^2 \gamma} W^2 + \frac{eV_0}{2\pi}\left[\cos\phi_s - \cos\phi - (\phi - \phi_s)\sin\phi_s\right]\,. \tag{71}$$

Curves of H = constant in the longitudinal ϕ–W phase plane represent the particle trajectories (Fig. 13). We see that the curves are closed for small deviations from the synchronous condition $(\phi_s, 0)$, indicating stable *synchrotron oscillations* about this point. In fact there are two distinct situations, depending on whether the energy is below or above transition.

Below transition $\gamma < \gamma_t$, the parameter $\eta > 0$, and the synchronous phase occurs on the rising side of the rf voltage wave ($0 \le \phi_s \le \pi/2$). The reason for this becomes clear if the motion is followed in detail in the phase plane. For a particle lagging behind in phase ($\phi > \phi_s$) the accelerating voltage will be higher on the rising side (since $\sin\phi > \sin\phi_s$ there) and hence by (68) the energy difference ΔE will grow more positive. But according to (69) $\Delta E > 0$ will lead to a faster orbit ($d\phi/dt < 0$) and negative phase change (a succession identifiable as the first quadrant of a counterclockwise orbit in the phase plane) —*provided* $\eta > 0$, that is, below transition.

Above transition, where η is negative, slower orbits and negative phase change are contrariwise produced by negative ΔE. In this case stable orbits require $\sin\phi < \sin\phi_s$ (for $\phi > \phi_s$) and hence the synchronous phase occurs on the falling side of the voltage wave ($\pi/2 \le \phi_s \le \pi$). The trajectories in the phase plane are mirror images of those for $\gamma < \gamma_t$.

The differential equation for the phase oscillation may be obtained by eliminating $\Delta E/\omega_0$ between (68) and (69):

$$\frac{d^2\phi}{dt^2} = -\frac{heV_0}{2\pi R_0^2 m_0}\frac{\eta}{\gamma}(\sin\phi - \sin\phi_s)\,. \tag{72}$$

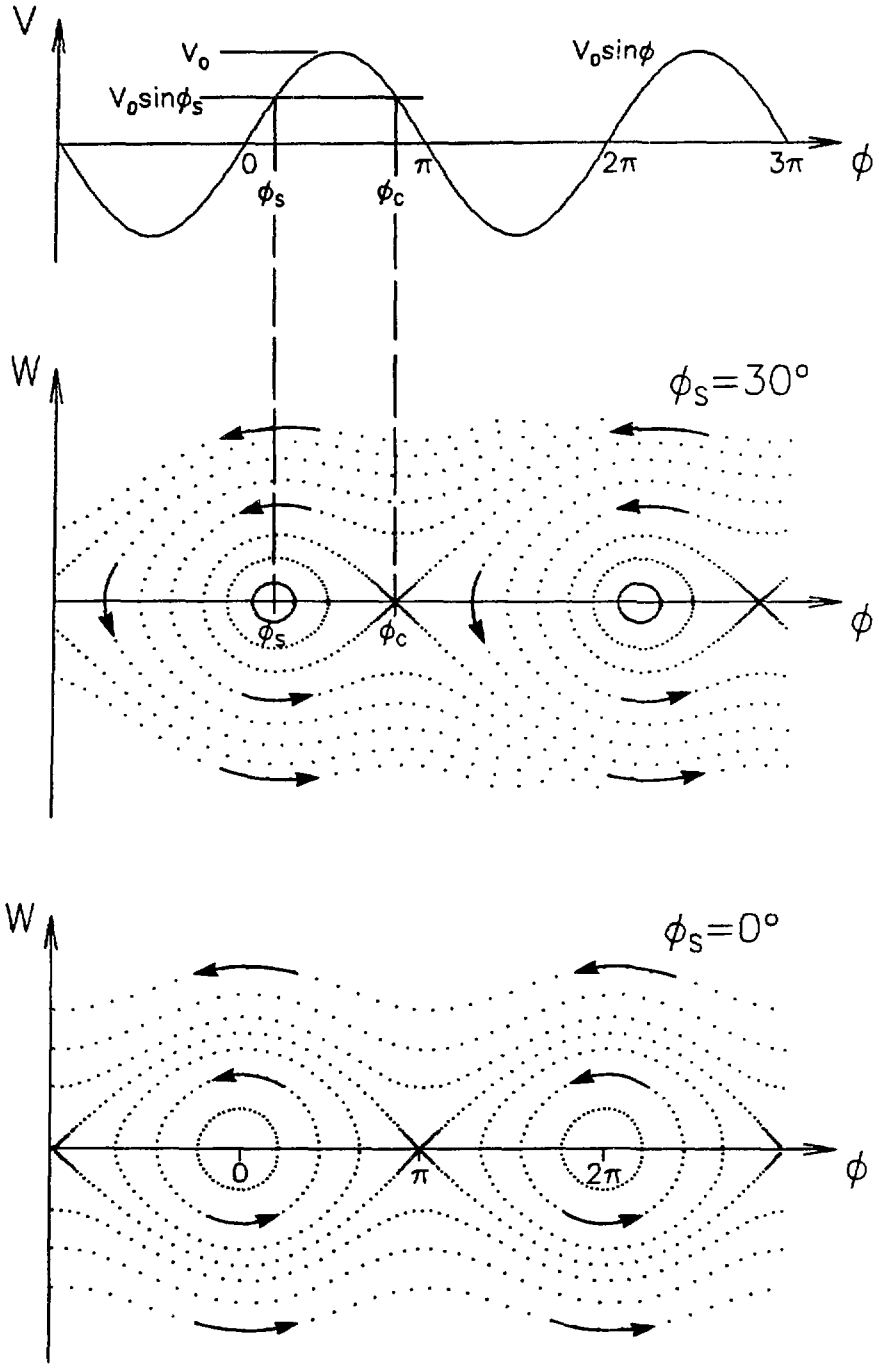

Figure 13: Stroboscopic view of particle trajectories in the W–ϕ phase plane; the dots are plotted at equal time intervals.

For large deviations from ϕ_s, the restoring force is clearly non-linear, due to the sinusoidal voltage variation. For small deviations, however, the force is linear in $(\phi - \phi_s)$, resulting in a simple harmonic oscillation at a frequency $\nu_s\omega_0$, where ν_s is the "synchrotron tune," given by (***Exercise 21***)

$$\nu_s = \sqrt{\frac{h}{2\pi} \cdot \frac{eV_0 \cos\phi_s}{m_0c^2} \cdot \frac{|\eta|}{\beta^2\gamma}} \,. \tag{73}$$

Because $eV_0 \ll m_0c^2$, the tune $\nu_s \ll 1$, so that particles take tens or hundreds of turns to complete a synchrotron oscillation. (Even so the oscillations are much faster than the rates at which ω_0, p_0, η, V_0 and ϕ_s change, so that our tacit assumption of their constancy has been reasonable.) Note that the tune varies strongly with energy, reaching zero at transition, where the oscillations come to a standstill.

For large deviations from the synchronous condition the trajectories do not close, and the motion becomes unstable, W becoming more and more negative as the particle is left behind the accelerating bucket. A pear-shaped separatrix divides the unstable region from the stable "bucket," whose area gives the longitudinal acceptance of the machine.

The width of the bucket can be shown to depend on ϕ_s alone. The phase of the cusp ϕ_c is simple to evaluate. Like the minima of the unstable trajectories it occurs where $dW/dt = 0$. From (68) this implies that

$$\phi_c = \pi - \phi_s \tag{74}$$

so a phase oscillation may extend over the top of the voltage wave to the point where V has dropped to $V(\phi_s)$. Inserting the coordinates of the cusp $(\phi, W) = (\pi - \phi_s, 0)$ in (71) we may obtain (***Exercise 22***) the value of the constant H for the separatrix and hence the height of the bucket:

$$\widehat{W} = W(\phi_s) = \sqrt{\frac{m_0R_0^2eV_0\gamma}{\pi h\eta}[2\cos\phi_s - (\pi - 2\phi_s)\sin\phi_s]} \,. \tag{75}$$

For a given value of ϕ_s the bucket height and area may be seen from (75) to be proportional to $\sqrt{V_0\gamma/|\eta|}$. The equation for the separatrix may also be used to obtain the extreme phase ϕ_e at the opposite end of the bucket to the cusp, by setting $W = 0$ and solving the resulting transcendental equation

$$\cos\phi_e + \phi_e \sin\phi_s = (\pi - \phi_s)\sin\phi_s - \cos\phi_s \,. \tag{76}$$

Neither ϕ_e nor the area of the bucket can be expressed in terms of simple functions of ϕ_s, but tabulated numerical values are available (see *e.g.* Bovet *et al.*, 1970).

Below transition the range of synchronous phases extends down to $\phi_s = 0$. This extreme value is symmetrically placed on the voltage wave, and consequently the bucket for this case is mirror-symmetric (Fig. 13). One cusp occurs at $\phi_c = \pi$ and another at $-\pi$ (otherwise regardable as the $+\pi$ cusp of the neighbouring bucket). The net effect is that the stable region extends over the complete 2π (at $\Delta E = 0$) —at the price of there being zero energy gain, averaged over a complete synchrotron oscillation. This is not an academic curiosity, but a useful mode for accumulation, capture or storage of a beam at constant energy. Above transition the corresponding condition occurs for $\phi_s = \pi$.

As ϕ_s is increased from 0 (or decreased from π) towards $\pi/2$, the width, height and area of the stable bucket all decrease towards zero, for given values of γ, η and V_0. Indeed (74)

shows that ϕ_c and ϕ_s become coincident for $\phi_s = \pi/2$. Thus the condition for maximum energy gain completely removes phase stability! To achieve adequate stable bucket area a lower energy gain per turn must be accepted. From a beam dynamics point of view the optimum values for synchronous phase $\phi_s(t)$ and rf voltage $V_0(t)$ at each point in the cycle can be determined uniquely from the required energy gain per turn (66) and bucket area. In practice other considerations, particularly rf engineering ones, may prevail. A value of ϕ_s around 30° (150°) is often used.

For most existing proton synchrotrons the transition energy lies within the acceleration range. In approaching γ_t at constant ϕ_s and V_0 the width of the bucket remains constant but its height and area increase as $\sqrt{\gamma/|\eta|}$, i.e. towards infinity. For a bunch of particles the emittance area will remain unchanged, but the aspect ratio will follow that of the bucket, at least at first; as a result the bunch length will shrink as $(|\eta|/\gamma)^{1/4}$ and its momentum spread will increase as $(\gamma/|\eta|)^{1/4}$. These effects reach a natural limit as the rate of rise of the bucket becomes too fast for the bunch to follow adiabatically, the synchrotron motion becoming increasingly sluggish as the tune $\nu_s \to 0$. Nevertheless both effects are sufficiently large to be undesirable. The bunching enhances longitudinal space charge effects (see below), firstly a change in bucket area across transition, causing mismatch, and secondly microwave instabilities. The increased momentum spread requires tighter tolerances on chromaticity and stopband width. In order to minimize these effects it has been usual to programme γ_t with a sudden jump so that no time is spent close to the transition condition. At the same moment the rf phase must be shifted by $\pi - 2\phi_s$ so that the bunch finds itself on the falling side of the rf wave, the stable side above γ_t.

Isochronous cyclotrons operate right on transition at all energies, in the sense that $\eta = 0$ and the orbital frequency is independent of momentum and phase. (No transitions are necessary, of course, so the terminology is redundant.) Under these conditions the analysis above breaks down. There is no special synchronous phase ϕ_s (all phases are equally synchronous) and no stable bucket. In a W–ϕ phase plane defined for some reference energy, the representative points are stationary. In an E–ϕ phase plane the points move up in energy at fixed phase according to (67). After $n = \omega_0 t/2\pi$ orbits starting from injection energy E_i the ion energy is given by

$$E = E_i + neV_0 \sin\phi\,. \tag{77}$$

While (69) suggests that $d\phi/dt = 0$ for $\eta = 0$, Joho (1974) has pointed out that another effect must be considered if the accelerating voltage varies with radius so that $V_0 = V_0(R)$. In this case the longitudinal rf electric field will be accompanied by a vertical rf magnetic field $B_0(R)$ which will modify the orbital frequency and lead to a variation of phase with radius and energy $\phi(E)$. In place of (71) above we have the Hamiltonian

$$H(\phi, E) = -\frac{eV_0}{2\pi}\cos\phi\,, \tag{78}$$

which defines the flowlines in the longitudinal phase plane. These are illustrated in Fig. 14, which shows how a decreasing $V_0(R)$ produces a "phase expansion" effect. Beam emittance is conserved since the stretching in phase is balanced by compression in energy. The example is taken from Joho's proposal (1984) for the ASTOR 2 GeV isochronous cyclotron, to be used as an intermediate stage between the SIN 590 MeV cyclotron and a 20 GeV high-intensity proton synchrotron. ASTOR would compress 250-turn packets into a small enough radial

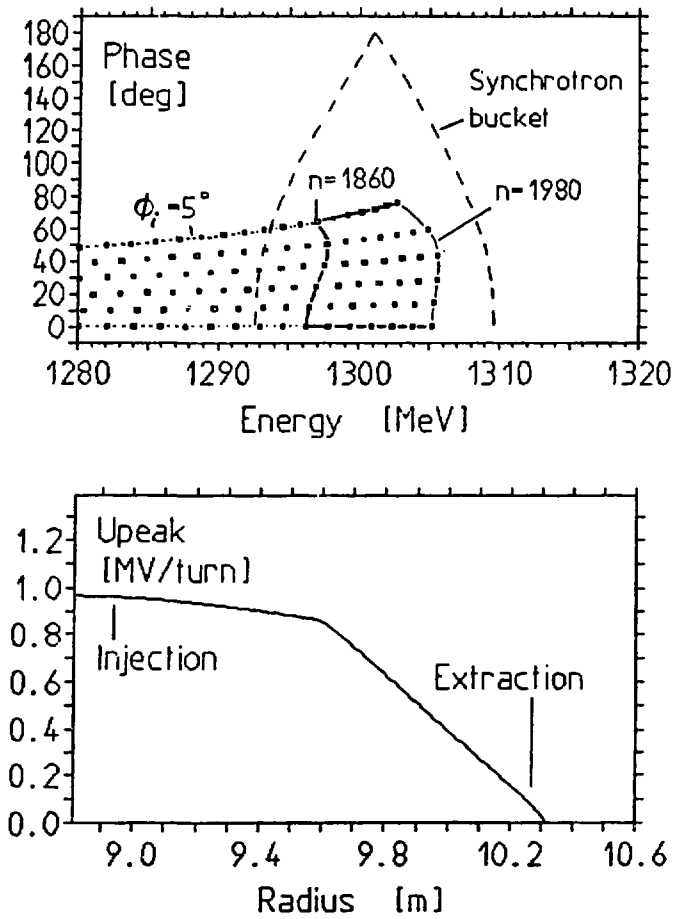

Figure 14: Phase expansion and energy compression (above) with a radially decreasing accelerating voltage (below). The phase width of the beam increases from ±5° at injection to ±75° at extraction.

interval for efficient extraction, while leaving them with a suitable phase-energy distribution to match and partly fill the synchrotron buckets.

LONGITUDINAL SPACE CHARGE EFFECTS

Any variation in density along the orbit (i.e. bunching) will produce longitudinal electric fields which will modify the accelerating voltage $V_0 \sin \phi$ provided by the rf cavities, changing the phase focusing strength and bucket area, and possibly producing instabilities. The longitudinal component of electric field derives both from the direct space charge of the beam and from the (opposite) charge induced on the surrounding surfaces. For simplicity we assume that both the beam and vacuum chamber are of circular cross-section, with radii a and w respectively (Fig. 15). The transverse fields within the beam are given by (45) and

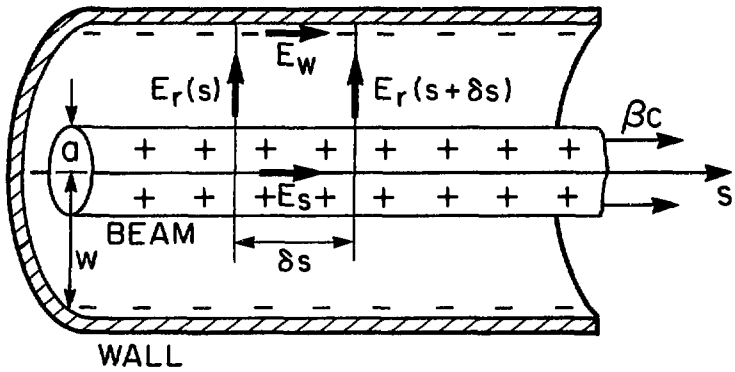

Figure 15: Longitudinal space charge fields.

(46), those outside the beam by

$$E_r = \frac{e\lambda}{2\pi\varepsilon_0}\frac{1}{r} \tag{79}$$

$$B_\phi = \frac{\mu_0 e\lambda v}{2\pi}\frac{1}{r} \tag{80}$$

where $\lambda(s) = dN/ds = \pi a^2\rho/e$ represents the numerical line density. In order to evaluate the electric field component E_s along the axis (***Exercise 23***) we use the integral form of Faraday's Law of Magnetic Induction over a rectangular path ($w \times \delta s$) from axis to wall and back, obtaining

$$E_s = -\frac{eg_0}{4\pi\varepsilon_0\gamma^2}\frac{d\lambda}{ds} + E_w\,, \tag{81}$$

where

$$g_0 \equiv 1 + 2\ln\frac{w}{a} \tag{82}$$

and E_w is the longitudinal field at the wall. This drives the wall current I_w, which is equal in magnitude but opposite in sign to the a.c. component of the beam current. In most accelerators the reactive wall impedance is inductive at low and medium frequencies. Denoting the total inductance around the machine by L, the wall field

$$E_w = \frac{L}{2\pi R}\frac{dI_w}{dt} = \frac{ev^2L}{2\pi R}\frac{d\lambda}{ds}\,. \tag{83}$$

Thus both space charge and wall contributions to the longitudinal field E_s experienced by a particle on the axis are directly proportional to the charge density gradient in its vicinity, so that overall

$$E_s = -\frac{e}{4\pi R}\left[\frac{g_0 R}{\varepsilon_0\gamma^2} - \beta^2c^2L\right]\frac{d\lambda}{ds}\,. \tag{84}$$

The two effects act in opposition, the wall being inductive and dominant at high energy, the space charge capacitive and dominant at low energy. Over one complete orbit (for which the synchrotron motion is negligible) the particle will experience an effective voltage

$$\Delta V(\phi) = 2\pi R E_s = e\beta c\frac{d\lambda}{d\phi}h\left[\frac{g_0 Z_0}{2\beta\gamma^2} - \omega_0 L\right] \tag{85}$$

where $Z_0 = 1/c\varepsilon_0 = 377\Omega$. Note that, for better comparison with cavity voltages, the density gradient has been expressed in terms of its time variation at an accelerating gap rather than its spatial variation at an instant; the sign change occurs because more positive s corresponds to more negative ϕ (leading particles arrive early).

The expression in square brackets in (85) represents the effective impedance at the orbit frequency ω_0; the factor h describes the increased impedance at the bunch frequency $h\omega_0$. To maintain a formula applicable to any harmonic frequency $n\omega_0$ it is usual to define

$$\frac{Z_e}{n} \equiv j\left[\omega_0 L - \frac{g_0 Z_0}{2\beta\gamma^2}\right] . \tag{86}$$

At low energies the capacitive space charge term predominates. The induced voltage $\Delta V(\phi)$ therefore swings from positive to negative, just like $d\lambda/d\phi$, as ϕ passes through the phase for which λ is a maximum — ϕ_s for any single-peaked time-invariant particle distribution (Fig. 16). If the energy is also low enough to be below transition ($\gamma < \gamma_t$), ϕ_s will lie on the rising side of the rf voltage wave $V(\phi)$, and the net effect of $\Delta V(\phi)$ will be to decrease the slope of the rise around ϕ_s. But from (72) and (73) we see that the synchrotron restoring force is proportional to this slope, and the synchrotron tune ν_s to its square root. The space charge $\Delta V(\phi)$ will thus reduce them both. The stable bucket and the bunch contour will also shrink in height and area, as V_0 is in effect decreased.

To be more specific we follow Hofmann and Pedersen (1979) in considering (***Exercise 24***) a particle distribution which is elliptic in energy

$$g(W,\phi) \equiv \frac{d^2N}{dW\,d\phi} \propto \sqrt{W_b^2(\phi) - W^2} \tag{87}$$

where $W = W_b$ on the bunch boundary in phase space. From (71) we see that the density $g(W,\phi) = g(H)$ remains invariant in time as the particles flow along lines of constant H in phase space. Integrating over W to obtain the line density

$$\lambda(\phi) = \frac{h}{R}\frac{dN}{d\phi} \propto W_b^2(\phi) \tag{88}$$

we find the same phase dependence as in (71). The density gradient therefore has the same shape as the applied voltage (relative to $V_s \equiv V(\phi_s)$ — see Fig. 15)

$$\frac{d\lambda}{d\phi} \propto V_0 \sin\phi - V_0 \sin\phi_s . \tag{89}$$

From (85) so also does the space-charge induced voltage $\Delta V(\phi)$, and as a result the total voltage V_t can be written

$$V_t(\phi) \equiv V_s + k_t[V(\phi) - V_s] \tag{90}$$

where

$$k_t \equiv 1 + 2\pi h \frac{\bar{I}}{V_0}\frac{Im(Z_e/n)}{f(\phi_1,\phi_2)} \tag{91}$$

and

$$f(\phi_1,\phi_2) = \sin\phi_2 - \sin\phi_1 - \frac{1}{2}(\phi_2 - \phi_1)(\cos\phi_1 + \cos\phi_2) , \tag{92}$$

The magnitude of the voltage change, described by the factor k_t, is seen to depend directly on the time-averaged beam current $\bar{I}$ and the effective impedance $h(Z_e/n)$, and inversely

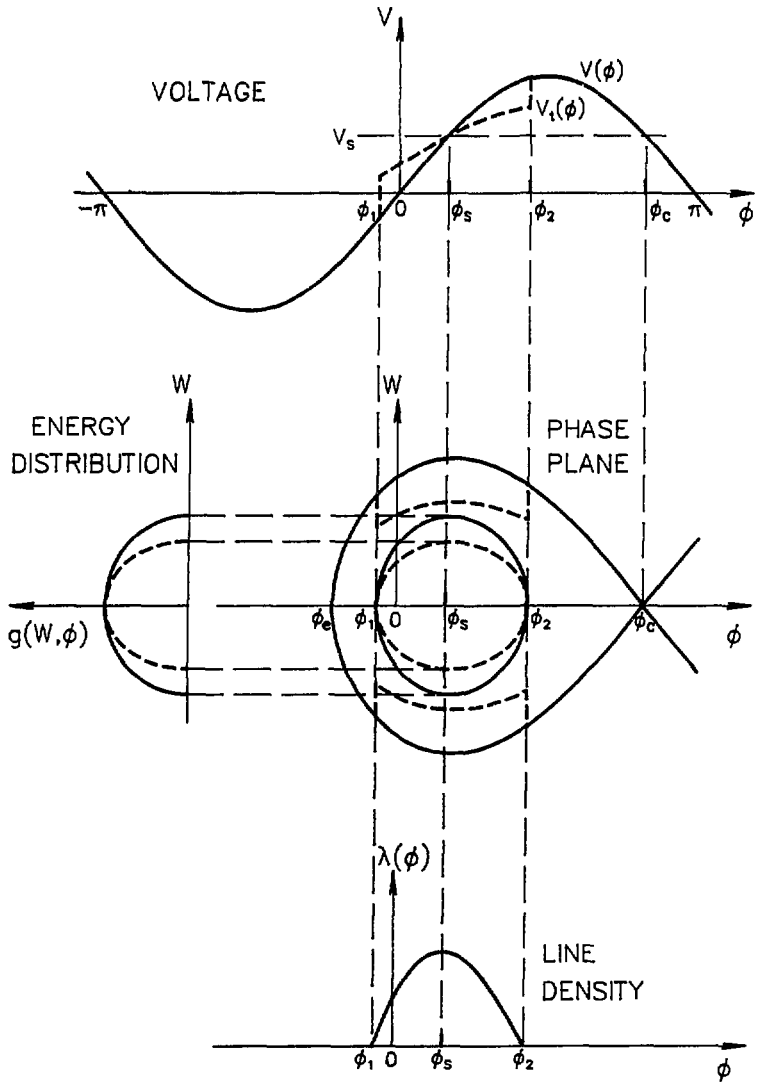

Figure 16: Effect of space charge in a beam bunch on the rf voltage and bucket: with (— — —) and without (————) space charge.

on the applied voltage V_0 and the function $f(\phi_1, \phi_2)$, which depends on the phase values at the ends of the bunch ($\phi_1 \leq \phi \leq \phi_2$) and grows with its length $\phi_l = \phi_2 - \phi_1$. For very short bunches

$$f(\phi_1, \phi_2) = \frac{1}{12}\phi_l^3 \cos\phi_s \,. \tag{93}$$

At low energies the (capacitive) impedance is negative and so $k_t < 1$ and $dV/d\phi$ is reduced as described above. As a result the heights of the bucket and of the other contours of constant H, including the bunch boundary, are reduced proportional to $\sqrt{k_t}$ over the

length of the bunch. The same is true for the area occupied by the bunch:

$$\frac{A_t}{A} = \frac{W_t(\phi)}{W(\phi)} = \sqrt{k_t}\,. \tag{94}$$

Beyond the ends of the bunch the voltage, the bucket shape and the H contours are unaffected. The change is not completely abrupt at the ends of the bunch, although it appears to be so in our simple model in which fringing fields are neglected. Of course, if the bunch fills the whole bucket then (94) applies to its area too.

From (91) it would appear that for a sufficiently high beam current the bucket would be completely suppressed. In practice high-frequency *instabilities* will develop within the bunch before the space charge limit is reached. Instabilities are treated in a later lecture by J.-L. Laclare (1986). For present purposes it will be sufficient to quote the Keil-Schnell criterion (1969) for the stability of coasting (uniform) beams, as applied by Boussard (1975) to bunched beams:

$$I(\phi) \leq F' \frac{|\eta|}{e\beta^2 E} \frac{[\Delta E(\phi)]^2}{|Z_e'/n|}\,. \tag{95}$$

Here F' is a form factor, Z_e'/n is the microwave coupling impedance, and $\Delta E(\phi)$ refers to the full width of the energy distribution at half height (FWHH). The criterion sets a current threshold for microwave instability, which in general will vary along the bunch. For the elliptic energy distribution, however, we know from (88) that the local charge density is proportional to the square of the local energy spread, so that in this case the criterion is independent of phase. Evaluating the microwave threshold current for the reduced voltage given by (90), and substituting it back in (91) to get the corresponding k_t, Hofmann and Pedersen find (***Exercise 25***) that most of the physical quantities cancel out, leaving an almost purely numerical expression:

$$k_t = \left[1 + \frac{3F'}{\pi} \frac{Im(Z_e/n)}{|Z_e'/n|}\right]^{-1}\,. \tag{96}$$

For not too short bunches and well-damped resonance the impedance at high frequency and reactance at low frequency may be assumed roughly equal, leading to $k_t \simeq 0.6$ for $F \simeq 0.7$, *i.e.* the microwave instability will break in when the space charge induced voltage rises to about 40% of the applied voltage.

The numerical nature of (96) is a reflection of the similar forms of the instability criterion (95) and the standard relation (75) between bucket height and rf voltage. Although dispersion relations are needed to derive (95), its similarity to (75) is suggested by some elementary considerations. The criterion must express the balance between driving and damping mechanisms, the former described by the induced voltage IZ_e, the latter by the spread in orbital frequencies $\Delta\omega$ which inhibits coherent motion through Landau damping. The frequency spread is provided by the momentum spread ($\Delta\omega/\omega = \eta\Delta p/p$) and hence the criterion is of bucket height–voltage form.

So far we have considered only energies low enough to be below transition ($\gamma < \gamma_t$) and to give capacitive coupling impedances. For these conditions $k_t < 1$ and the rf voltage and bucket height are reduced. But in fact the same effects result at high energies—provided they are high enough to be simultaneously above transition ($\gamma > \gamma_t$) and to give inductive impedances. While the impedance change reverses the sign of $\Delta V(\phi)$, the shift of the

synchronous phase to the falling side of the rf voltage wave again produces a reduction in the slope of the voltage.

At intermediate energies, however, there is the possibility of the opposite situation. Either below γ_t with inductive Z_e, or above γ_t with capacitive Z_e, the slope of the voltage is increased, $k_t > 1$ and the bucket grows bigger. The energy for impedance reversal is determined by the inductance and the pipe/beam diameter ratio w/a:

$$\beta\gamma = \sqrt{\frac{g_0 Z_0}{2\omega_c L}}, \tag{97}$$

where $\omega_c = c/R_0$. With $\omega_c L \simeq 10\Omega$, typical of well engineered machines, and $w/a = e$ ($g_0 = 3$), we obtain $\beta\gamma = 7.5$. This is close to γ_t for 30 GeV machines like the CERN PS and Brookhaven AGS. For higher energy machines, however, γ_t is higher, and there exists a significant energy range over which the bucket will increase rather than decrease in height. (Efforts to reduce $\omega_c L$, for instance to $< 1\Omega$, will of course narrow this range). As the bucket grows taller the beam bunch will tend to follow its shape and grow narrower; this narrowing of the bunch as a result of space charge represents a "negative mass" effect.

We are now in a position to explain the perils of crossing transition, alluded to above, in more detail. Firstly, the switch in synchronous phase from the rising to the falling side of the rf wave will produce an abrupt change of sign in $f(\phi_1, \phi_2)$ and hence in $k_t - 1$; the resulting sudden jump in bucket height will leave the bunch mismatched. Secondly, the bucket height decrease/increase is greatest near transition, making the beam more susceptible to microwave instabilities. Recent designs for very high intensity proton synchrotrons (kaon factories) have tended to avoid crossing transition altogether by driving $\gamma_t \gg \nu_x$ (or $\ll \nu_x$). In some cases this results in enhanced rf voltage and bucket height over a large energy range.

BEAM BRIGHTNESS AND MULTISTAGE ACCELERATORS

Modern high energy proton accelerators consist of several synchrotron stages following an injector, normally a linac. Table I lists the energies of the various stages for existing and (below the dashed line) proposed machines.

There are a number of reasons for breaking these accelerators into stages, each with a restricted energy range. One is to avoid operating the magnets in a very low field region where field quality and control is poor. A second, especially important for rapid-cycling machines, is to separate the lower energies (say below 3 GeV, where $\beta \simeq 0.97$) where a large swing in radiofrequency is required, from the main energy range, where a high rf voltage must be provided. A third, of particular concern in high intensity machines, and therefore worthy of elaboration here, stems from the space-charge induced shift $\Delta\nu$ in betatron tune, given by (52) or (54). The sharp rise in $\Delta\nu$ with decreasing energy ($\Delta\nu \propto N/\varepsilon^*\beta\gamma^2$) and the need to keep its magnitude below about 0.2 to avoid crossing fourth or lower order resonances, determine the minimum injection energy for a machine designed for charge Ne and emittance ε^*. If this is above the injector energy, a lower energy synchrotron stage is required, and so on...

For a chain of synchrotrons it is helpful to express the tune shift equation as far as possible in terms of quantities that are invariant through the chain. The normalized emittance ε^* is one such quantity, assuming no deterioration in beam quality during accel-

Table I: Multistage Proton Accelerator Energies

Institute	Injector	Stage 1	Stage 2	Stage 3	Stage 4
Brookhaven	200 MeV	1.5/2.5 GeV	33 GeV		
CERN	50 MeV	0.8 GeV	10/28 GeV	450 GeV	
Fermilab	200 MeV	8.0 GeV	150/500 GeV	1000 GeV	
KEK	40 MeV	0.5 GeV	12 GeV		
Serpukhov	100 MeV	1.5 GeV	76 GeV	600 GeV	3 TeV
DESY	50 MeV	7.5 GeV	40 GeV	820 GeV	
SSC	600 MeV	7 GeV	100 GeV	1000 GeV	20 TeV
TRIUMF	450/520 MeV	3 GeV	30 GeV		
LAMPF	800 MeV	6 GeV	45/60 GeV		
EHF	1200 MeV	9 GeV	30 GeV		

eration or transfer between the stages. The number of particles N varies from ring to ring, but is related to another invariant, the average current passing through the system, $\overline{I} = eN_1/\tau_1 = eN_2/\tau_2 = \ldots$, where τ_i is the cycle time for the ith ring, and beam losses are assumed negligible. Equation (54) then shows that the tune shift for each ring is directly proportional to the time-averaged one-dimensional *beam brightness* $\overline{B_1^*} = \overline{I}/\varepsilon^*$ (invariant through the system), but depends also on terms peculiar to that ring:

$$\Delta\nu_i = -\frac{r_p \overline{B_1^*}}{\pi e}\left(\frac{FGH}{B_f}\cdot\frac{\tau}{\beta\gamma^2}\right)_i . \tag{98}$$

[Note that the *instantaneous* brightness B_1^* defined by (53) is not the appropriate quantity for a chain of synchrotrons, since it is not invariant; being based on the circulating current, it increases in direct proportion to particle velocity].

An alternative form for $\Delta\nu_i$ is obtained by writing $N = 2\pi R\overline{\lambda}$, where $\overline{\lambda}$ is the spatially averaged line density. This is also invariant from machine to machine, provided pulses from one ring are simply stacked end-to-end, box car fashion, in the next ring. The resulting expression is

$$\Delta\nu_i = -2r_p \cdot \frac{\overline{\lambda}}{\varepsilon^*}\left(\frac{FGH}{B_f}\cdot\frac{R}{\beta\gamma^2}\right)_i . \tag{99}$$

If the tune-shift at injection is limited to the same value at each stage, the term in parentheses will also take a constant value. Thus for each ring in a given chain

$$\left(\frac{B_f\beta\gamma^2}{FGH}\right)_{\text{inj}} = \frac{2r_p}{|\Delta\nu|}\frac{\overline{\lambda}}{\varepsilon^*}R \propto R; \tag{100}$$

there is a fixed relation between conditions at injection and the average radius R. Since this is a parameter determined by the top energy, (100) defines the energy range for each stage. In terms of the top momentum

$$(\beta\gamma^2)_{\rm inj} = \frac{2m_0cr_p}{e(\rho/R)}\frac{\overline{\lambda}}{\varepsilon^*}\left(\frac{FGH}{B_f|\Delta\nu|}\right)_{\rm inj}\left(\frac{\beta\gamma}{B}\right)_{\rm max} \tag{101}$$

where ρ/R is the dipole packing fraction and B is the dipole magnetic field strength. In so far as we can neglect variations in the various parameters from ring to ring, we may write

$$(\beta\gamma^2)_{\rm inj} = k(\beta\gamma)_{\rm max}\,. \tag{102}$$

In practice we can only expect k to be very roughly constant from stage to stage. Even if $\Delta\nu$ is the same for each ring, the packing fraction will vary with the lattice, $B_{\rm max}$ will depend on the cycling rate, and the bunching factor B_f will probably be larger for the first stage than for subsequent ones.

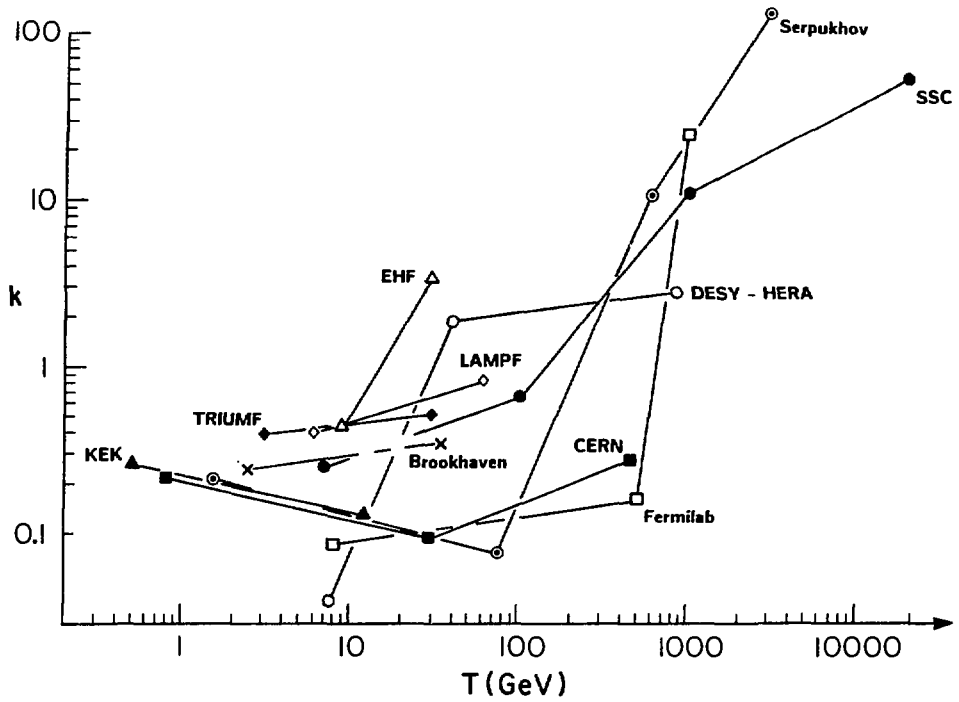

Figure 17: Values of the parameter $k = (\beta\gamma^2)_{\rm inj}/(\beta\gamma)_{\rm max}$, plotted against energy for each stage of various multistage machines.

Values of k for a number of multistage machines are plotted in Fig. 17. For most lower energy stages k is constant within a factor 2. Higher intensity machines tend to have "shorter" stages and higher k values, presumably reflecting the use of brighter beams or more conservative $\Delta\nu$. Large changes in k show where $\Delta\nu$ was not critical in choosing the staging energies—where tunnels already existed (DESY-HERA), to avoid depolarization (EHF) and for very high energies. The case of the proposed SSC is an interesting one. Here

considerations of tune shift and beam brightness (Ankenbrandt, 1984) led to a decision to add a third Low Energy Booster (LEB) to the original two booster stages. With the energies of the original stages more or less fixed, however, the tune shift is only critical in the LEB, and k increases strongly with energy.

HIGH INTENSITY PROTON SYNCHROTRONS

Ever since the first proton synchrotrons were built 30 years ago there has been a steady effort to increase primary beam intensity and hence the fluxes of secondary particles (kaons, antiprotons, neutrinos, *etc.*) and the capability of studying rarer and rarer particle interactions. The most recent initiative has been the proposal of a new generation of fast-cycling synchrotrons—the so-called kaon factories—machines with beam intensities a hundred times greater than those available at present.

In considering the maximum intensity which can be accelerated in a synchrotron two parameters are of particular importance, the number of particles per pulse N and the circulating current I. N is critical because it determines the incoherent space charge tune shift $\Delta\nu$, given by (54), the decrease in the betatron tune due to the defocusing effects of space charge. Of course, a drop in tune by itself could be compensated by adjusting the quadrupole magnets: the problem here is that the shift can vary across and also along the bunch, so that $\Delta\nu$ also represents a spread in tunes. In order to avoid coming too close to lower-order resonances it is generally agreed that $\Delta\nu$ should be kept below 0.2. The factor $\beta\gamma^2$ makes this condition most critical near injection. It was to take advantage of this energy dependence that the injection energies of the Brookhaven AGS and CERN PS were raised from the original 50 MeV to 200 MeV and 800 MeV, respectively. The crucial role $\Delta\nu$ plays in the design of multistage accelerators was discussed in the previous section.

The circulating current I is important through its involvement in longitudinal space charge effects and beam stability. We saw above how the current appears directly in Eq. (91) for k_t, the factor describing the effect of space charge on bucket height, and in (95), the Keil-Schnell-Boussard criterion for microwave stability.

The energy and intensity parameters, including N and $\bar{I}$, are listed in Table II for existing and proposed high energy proton synchrotrons. The existing higher energy machines achieve average beam currents of ~ 1 μA. These currents are limited both by the slow-cycling rate (< 1 Hz) and by their low injection energies (≤ 200 MeV into their first synchrotron stages) which restrict N to $\sim 2 \times 10^{13}$. The circulating current $I \simeq 1$ A.

Higher intensities have been achieved in machines using faster cycling rates (10–50 Hz). A record current (for a synchrotron) of 40μA was recently achieved at the Rutherford ISIS spallation neutron source, and this will be raised to 200 μA when commissioning is completed. The number of protons per pulse N will then be 2.5×10^{13}, only a little more than in the slow-cycling machines, but the circulating current $\bar{I}$ will rise to 6 A.

The proposed kaon factories aim at energies in the 25–45 GeV range with proton currents of 30–100 μA. Proposals have come from all three existing pion factories at LAMPF, SIN and TRIUMF, these laboratories being unique in already possessing operating machines with adequate energy and current to act as injectors, and also from a European consortium and from Japan. All the proposals also involve intermediate booster synchrotrons with energies in the 3–9 GeV range. These have a dual purpose. In the first place they raise the injection energy into the main ring, and therefore through Eq. (54) the charge per pulse

Table II: High-intensity proton synchrotrons.

	Energy (GeV)	Average current (μA)	Rep. rate (Hz)	Protons/ pulse N ($\times 10^{13}$)	Circulating current $\overline{I}$ (A)
Slow Cycling[a]					
KEK PS	12	0.32	0.6	0.4	0.6
CERN PS	26	1.2	0.38	2	1.5
Brookhaven AGS	28.5	0.9	0.38	1.6	0.9
—with Booster		(3)		(5)	(3)
Fast Cycling[b]					
Argonne IPNS	0.5	8	30	0.17	2.3
Rutherford ISIS	0.55(0.8)	40(200)	50	(2.5)	(6.1)
Fermilab Booster	8	7	15	0.3	0.3
AGS Booster	(1.5)	(20)	(10)	(1.25)	(3)
Proposed Boosters[b]					
TRIUMF	3	100	50	1.2	2.7
European HF	9	100	25	2.5	2.5
LAMPF	6	144	60	1.5	2.2
KEK Booster	1-3	100	15	4	8
Kaon Factories[a]					
TRIUMF	30	100	10	6	2.8
European HF	30	100	12.5	5	2.5
LAMPF	45	32	3.33	6	2.2
Japan—Kyoto	25	50	30	1	0.5
Japan—KEK	30	30	1	20	7

[a]Slow extraction
[b]Fast extraction

that can be accelerated, to $N \sim 6 \times 10^{13}$ ppp. This enables the desired current of 100 μA to be achieved with only moderately fast cycling rates $\sim$ 10 Hz. The second reason for using a booster synchrotron concerns the radio-frequency acceleration requirements. In a fast-cycling machine the much more rapid acceleration requires a much higher rf voltage than has been conventional at slower cycling rates—about 2 MV for a 10 Hz 30 GeV machine. At the same time a large frequency swing (20–30%) is required when starting from pion factory energies of 500–800 MeV. The use of a booster enables these demands to be handled separately. Almost the entire frequency swing can be provided in the booster

at relatively low rf voltage, while the main ring provides the 2 MV with only a few per cent frequency swing. Being smaller, the booster must cycle faster (15–60 Hz) in order to fill the circumference of the main ring. The charge per pulse would be $N \sim 10^{13}$, comparable to existing machines injected in the same energy range. The circulating current in both booster and main ring would be $\bar{I} < 3$ A, a level which is not expected to present any problems.

Many of the design features required for these high energy high intensity machines are common to all the proposals; to avoid repetition and because I am most familiar with the TRIUMF design, I will describe its rationale in some detail, reporting only distinctive features in the other cases. Before doing this, however, it will be appropriate to discuss the project already under construction at Brookhaven to enhance the AGS performance by the addition of a booster synchrotron.

BROOKHAVEN AGS BOOSTER

Funding for the booster began in October 1985 and the project is expected to be complete by the end of 1989. This is in fact a multi-purpose project aimed at the acceleration of heavy ions as well as polarized and unpolarized protons (Brookhaven, 1984; Lee, 1985). The booster ring is one-quarter the circumference of the AGS and is located in the angle between the linac tunnel and the AGS ring. The modes of operation for various particles are illustrated in Fig. 18, where the time scale covers the 2.8 s of a single slow extracted pulse. For unpolarized protons four booster pulses would be injected at a 10 Hz repetition rate within a 300 ms flat bottom, enabling the present 1.6×10^{13} ppp to be increased to 5×10^{13} ppp.

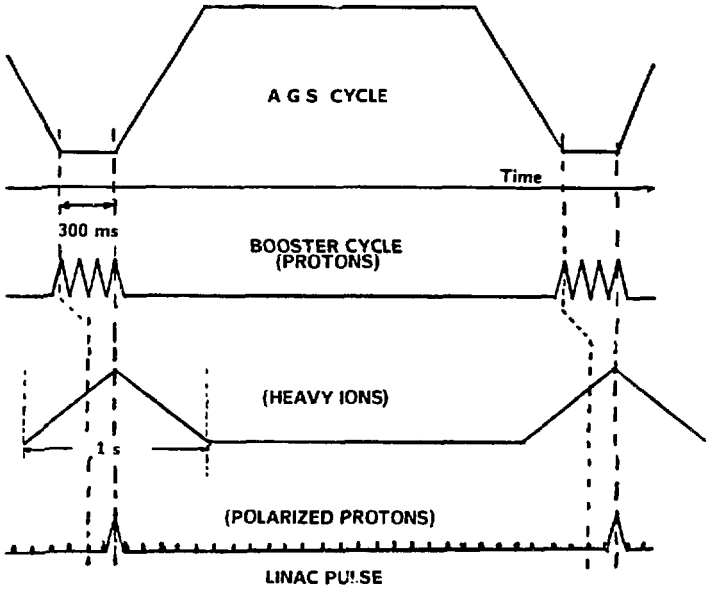

Figure 18: Injection programs for the AGS.

Initially protons would be accelerated to 1.5 GeV although the bending capability provided for heavy ions would eventually allow protons to be accelerated to 2.5 GeV. For heavy ions a slower acceleration time is required in the booster, and only one pulse would be injected into the main ring. For polarized protons there is the option of stacking up to 28 pulses in the booster ring before injecting them into the AGS. Further improvements beyond this program include the possibility of adding a 30 GeV stretcher ring and of making modifications to the AGS (rf, *etc.*) to accommodate $> 5 \times 10^{13}$ ppp and increase the beam intensity to as much as 2×10^{14} p/s (32 μA).

TRIUMF KAON FACTORY

The TRIUMF proposal (1985) is based on a 30 GeV main "Driver" synchrotron 1072 m in circumference accelerating 10 μC pulses at a 10 Hz repetition rate to provide an average beam current of 100 μA. For the reasons explained above a Booster synchrotron is used to accelerate protons from the TRIUMF cyclotron at 450 MeV to 3 GeV: this machine is 1/5 the radius of the main ring (Fig. 19) but cycles five times faster at 50 Hz. The Booster energy is chosen to minimize the total cost of the project. This depends mainly on magnet costs, and in particular on the magnet apertures. The minimum cost condition occurs when the emittances set by the space charge tune shift formula [Eq. (54)] are the same for both machines (Wienands and Craddock, 1986).

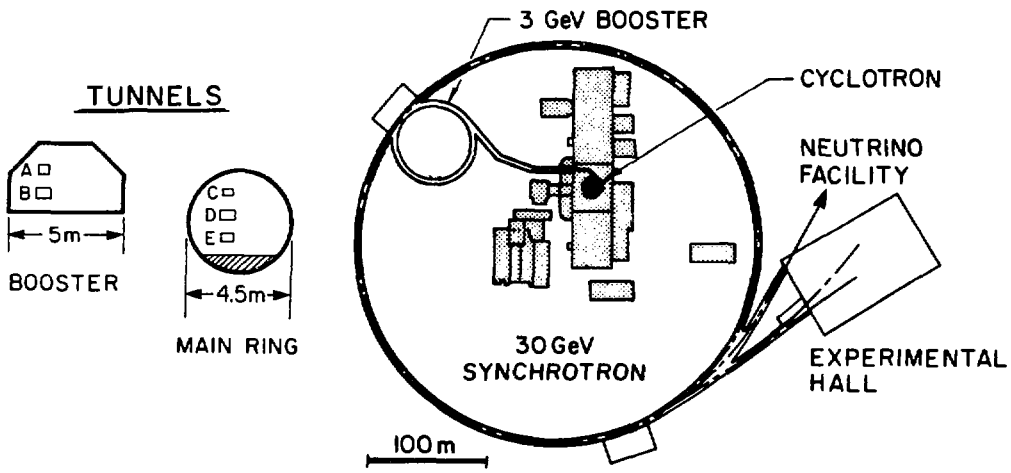

Figure 19: Proposed layout of the TRIUMF KAON Factory accelerators and cross sections through the tunnels.

Each of the three accelerators is followed by a dc storage ring to provide time-matching and finally a slow extracted beam for coincidence experiments. These are relatively inexpensive, accounting for only 25% of the total cost. Thus the TRIUMF cyclotron would be followed by a chain of five rings, as follows:

A	Accumulator:	accumulates cw 450 MeV beam from the cyclotron over 20 ms periods
B	Booster:	50 Hz synchrotron; accelerates beam to 3 GeV
C	Collector:	collects 5 booster pulses and manipulates the beam longitudinal emittance
D	Driver:	main 10 Hz synchrotron; accelerates beam to 30 GeV
E	Extender:	30 GeV storage ring for slow extraction

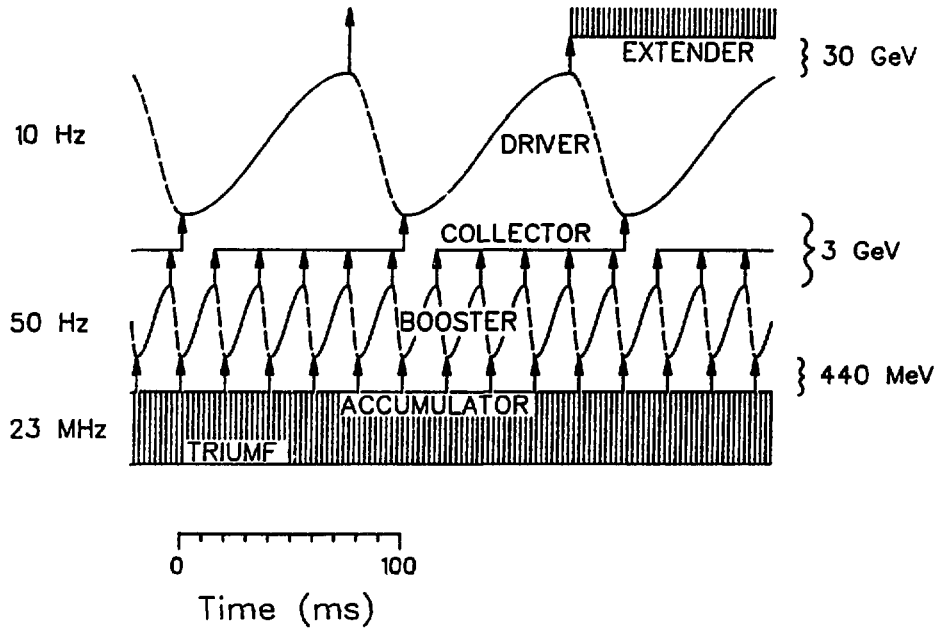

Figure 20: Energy-time plot showing the progress of the beam through the five rings.

As can be seen from the energy–time plot (Fig. 20) this arrangement allows the cyclotron output to be accepted without a break, and the B and D rings to run continuous acceleration cycles without wasting time on flat bottoms or flat tops; as a result the full 100 μA from the cyclotron can be accelerated to 30 GeV for either fast or slow extraction. Figure 20 also illustrates the asymmetric magnet cycles used in both synchrotrons. The rise time is three times longer than the fall, reducing the rf voltage required by 1/3, and the number of cavities in proportion. Full-scale power supplies providing such a cycle have been developed at Argonne (Praeg, 1983) with the encouragement of Los Alamos.

Figure 19 shows the location of the Accumulator directly above the Booster in the small tunnel, and of the Collector and Extender rings above and below the Driver in the

main tunnel. Identical lattices and tunes are used for the rings in each tunnel. This is a natural choice providing structural simplicity, similar magnet apertures and straightforward matching for beam transfer. Multi-ring designs are now conventional at the high-energy accelerator laboratories, and the use of bucket-to-bucket transfer at each stage rather than the traditional coasting and recapture should keep transfer spills to a minimum.

Separated function magnet lattices are used with a regular FODO quadrupole arrangement, but with missing dipoles arranged to give superperiodicity 6 in the A and B rings and 12 in the C, D and E rings. This automatically provides space for rf, beam transfer and spin rotation equipment. It also enables the transition energy to be driven above top energy in both synchrotrons, avoiding the beam losses usually associated with crossing transition in fast-cycling machines and the difficulties anticipated in making that jump under high beam-loading conditions. It will be recalled from (64) that the transition energy may be expressed roughly in terms of the momentum dispersion $\eta_x = \Delta x/(\Delta p/p)$ by $\gamma_t = \sqrt{R/\langle\eta_x\rangle}$, where R is the machine radius. In conventional alternating gradient proton synchrotrons with regular dipole lattices, $\eta_x \simeq$ constant and $\gamma_t \simeq \nu_x$. In a missing dipole lattice the dispersion function will oscillate (see Fig. 21) and its average value $\langle\eta_x\rangle$ can be driven down towards zero ($\gamma_t \to \infty$) or even to negative values (making γ_t imaginary). This effect can be enhanced, without perturbing the other lattice functions too strongly, by bringing the horizontal tune value ν_x towards, but not too close to, the integer superperiodic resonance. Values of $\nu_x \simeq 5.2$ for the $S = 6$ Booster and $\nu_x \simeq 11.2$ for the $S = 12$ Driver prove to be quite convenient. Associated choices of $\nu_y = 7.23$ and 13.22, respectively, keep the working points away from structural resonances and allow room for the anticipated space charge tune spreads, $\Delta\nu_y = 0.18$ and 0.11.

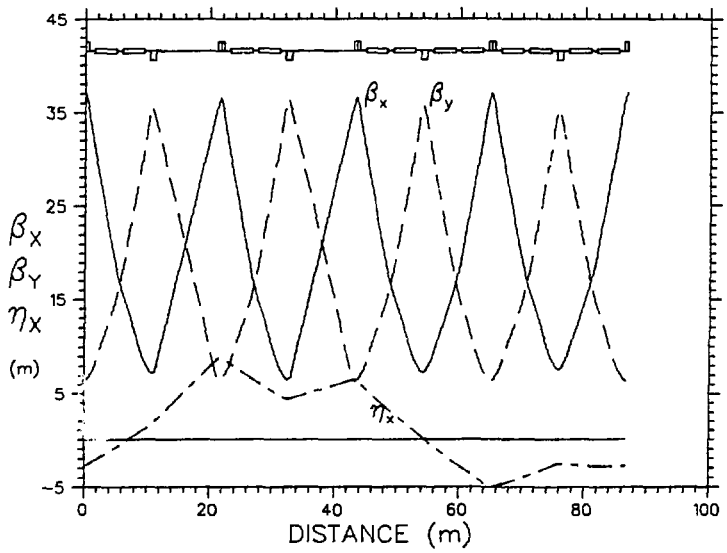

Figure 21: Magnet arrangement and lattice functions for the TRIUMF KAON Factory Driver synchrotron.

In fast-cycling machines the synchrotron tune ν_s is relatively large and care must be taken to avoid synchro-betatron resonances of the form

$$l\nu_x + m\nu_y + k\nu_s = n\,. \tag{103}$$

Here k, l and m are integers whose sum gives the order of the resonance, while n is an integer giving the Fourier harmonic of the field component driving it. Only the lowest order of these resonances, satellites of the integer betatron resonances, are of serious concern, but in the Booster ν_s is as large as 0.04, so that these could significantly reduce the working area available for the tune spread. Fortunately it is possible to mimimize their ill effects by suppressing the driving terms for the nearby integer resonances. This can be achieved by placing the rf accelerating cavities symmetrically with the magnet superperiodicity $S = 6$. The synchro-betatron resonances near $\nu_x = 5$ and $\nu_y = 7$ are then eliminated except for fifth harmonic variations in the cavity voltages and seventh harmonic errors in vertical dispersion.

The superperiodicity of the magnet lattice also drives *depolarizing* resonances. Compared to the AGS the superperiodicity is stronger but passage through the resonances is more rapid, so that the overall depolarizing effects are comparable in magnitude. At the higher energies it becomes impractical to build pulsed quadrupoles fast enough and strong enough to jump these resonances. Instead it is proposed to use helical "snakes" as proposed by E.D. Courant (1986). These would fit into the 10 m long drift spaces and cause a closed orbit distortion of < 4 cm at 3 GeV. Pulsed quadrupoles would be practical for the lower momenta resonances in the Booster.

At injection into the A and B rings the rf accelerating system will operate at 46.1 MHz, twice the radio frequency of the TRIUMF cyclotron. So that every other rf bucket is not missed the radius of these rings is made a half-integer multiple (4.5) of that of the last orbit in the cyclotron. The Booster cavities are based on the double gap cavities used in the Fermilab booster. They will develop a voltage of 26 kV at each gap for a frequency swing of 46–61 MHz. Twelve cavities will develop the required voltage of 580 kV. The cavities for the other rings are based on the single gap cavities designed for the Fermilab main ring. For the main synchrotron 18 cavities each developing 140 kV give a total of 2520 kV with a frequency swing from 61.1–62.9 MHz. To keep the rf power requirements within a factor two of the 3 MW beam power and to provide stability under high beam loading conditions, a powerful rf control system has been designed, based on experience at CERN, including fast feedback around the power amplifiers, and phase, amplitude, tuning, radial and synchronization feedback loops. One-turn-delay feedforward is used to control transient loading effects.

The Accumulator ring is designed to provide the matching between the small emittance cw beam from the TRIUMF cyclotron and the large emittance pulsed beam required by the Booster. The Accumulator will stack a continuous stream of pulses from the cyclotron over a complete 20 ms Booster cycle. Injection and storage over this 20,000 turn long cycle is only possible through the use of the H^- stripping process. This enables Liouville's theorem to be bypassed and many turns to be injected into the same area of phase space. In fact it is not necessary or desirable to inject every turn into the same area; the small emittance beam from the cyclotron [$(2\pi$ mm $\cdot$ mrad$)^2 \times 0.0014$ eV–s] must be painted over the much larger three-dimensional emittance $31 \times 93(\pi$ mm $\cdot$ mrad$)^2 \times 0.048$ eV–s needed in the Booster to limit the space charge tune shift [Eq. (54)]. Painting also enables the

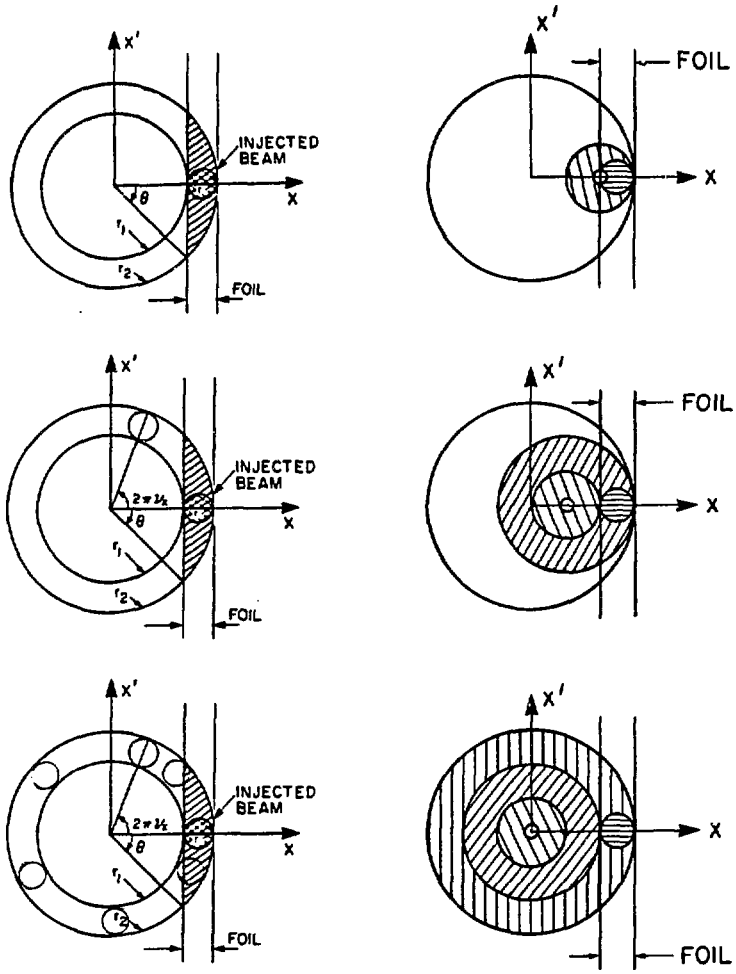

Figure 22: Painting the beam in the horizontal phase plane. Left: over many turns betatron oscillations will fill an annulus. Right: the central orbit is initially shifted to the edge of the stripping foil (and incoming beam spot) using bump magnets (top); their gradual deexcitation moves the C.O. (and stored beam) off the foil and back to the machine axis (bottom).

optimum density profile to be obtained and the number of passages through the stripping foil to be limited. The stripping foil lifetime is estimated to be > 1 day. The painting is achieved by a combination of magnetic field ramping (Fig. 22), vertical steering and energy modulation using additional rf cavities in the injection line. A group of 5 rf buckets (out of 45) will be left empty to provide $\simeq 100$ ns for kicker magnet rise and fall times during subsequent beam transfers.

At present, of course, the H^- ions are stripped in the process of extracting them from the cyclotron. To extract them whole from the cyclotron a new extraction system will be required, and elements of this have been under test for the last year. The first element is an rf deflector operating at half the fundamental frequency: it deflects alternate bunches in opposite directions. Because the cyclotron operates on an odd harmonic ($h = 5$) and the $\nu_x = 3/2$ resonance is nearby, this produces a coherent radial betatron oscillation. Although successive turns are not completely separated a radial modulation in beam density

is produced. An electrostatic deflector is then placed so that the septum is at a density minimum. In fact the septum is protected by a narrow stripping foil upstream so that no particles hit it; instead they are safely deflected out of the machine. The particles entering the electrostatic deflector eventually pass into magnetic channels and then into the Accumulator injection line. The magnetic channels have only just become available but tests with the first two elements have demonstrated 85% extraction efficiency.

Successful operation of a high-intensity accelerator depends crucially on minimizing beam losses and the activity they produce. Where some loss is expected, near injection and extraction elements, collimators and absorbers will be provided and equipment will be designed for remote handling. The beam current and any spill will be carefully monitored, and in case of the beam becoming unstable at any time through component failure or power excursions, each of the five rings is equipped with a fast-abort system which would dump the entire beam safely within one turn.

Several processes which give rise to losses in existing machines have been avoided entirely in this design. The use of H^- ions for injection into the Accumulator ring will almost entirely eliminate injection spill. The use of bucket-to-bucket transfer between the rings will avoid the losses inherent in capturing coasting beams. The buckets will not be filled to more than 60% of capacity; this should avoid beam losses while providing a sufficient bunching factor to minimize the space charge tune spread at injection and sufficient spread in synchrotron tune to give effective Landau damping. Magnet lattices are designed to place transition above top energy in all the rings, thus avoiding the instabilities and losses associated with that passage. Moreover, with the beam always below transition, it is no longer advantageous to correct the natural chromaticity, so that sextupole magnets are needed only for error correction, and geometric aberrations in the beam are essentially reduced to zero.

Beam instabilities will be suppressed or carefully controlled. Although all five rings have large circulating currents, the rapid cycling times give the instabilities little time to grow to dangerous levels. Coupled-bunch modes, driven by parasitic resonances in the rf cavities and by the resistive wall effect, will be damped using the standard techniques (Landau damping by octopoles, bunch-to-bunch population spread and active damping by electronic feedback). The longitudinal microwave instability is a separate case because of its rapid growth rate. It will be avoided by making the longitudinal emittance sufficiently large at every point in the cycle and by minimizing the high frequency impedance in the vacuum chamber as seen by the beam. At this stage of the design it is not possible to make accurate estimates of beam blow-up due to instabilities or non-linear resonances, but to be safe, the magnet apertures have been designed to accommodate a 50% growth in the horizontal, and 100% growth in the vertical beam emittance.

The proposal was submitted to TRIUMF's funding agencies, the National Research Council and the Natural Sciences and Engineering Research Council, in September 1985. The total cost, including salaries and E,D&I, but not contingency, is estimated to be M$427 (1985 Canadian dollars). Two review committees have been set up. The first, an international "Technical Panel" of particle, nuclear and accelerator physicists, met in February and has produced a very favourable report. The second "Review Committee" consisting of Canadian industrialists and scientists from various disciplines met recently and is expected to finalize its report later this summer.

LAMPF II

The Los Alamos proposal (1984, 1986) for a 45 GeV 32 μA facility aims at significantly higher energies but lower currents than the other schemes. It is argued that higher energy protons will be more suitable for Drell-Yan studies of quark confinement in the nucleus, besides providing higher momentum secondary beams. In fact it is aimed to achieve 60 GeV by running the main ring bending magnets at 2.0 T. Figure 23 shows the proposed layout, with the existing 800 MeV linac injecting every other H^- pulse into a 6 GeV circular booster synchrotron of circumference 330.8 m, operating at 60 Hz and providing an average current of 144 μA. Out of every 18 pulses, 14 (112 μA) are directed to Area N for neutrino studies, while 4 are transferred to the main ring of circumference 1333.2 m for acceleration to 45 GeV. With the magnets flat-topped for 50% of the cycle for slow spill to Area A, and a 3.33 Hz repetition rate, the average proton current is 32 μA. There are two modes of slow spill, either fully debunched with 100% microscopic duty factor, or with rf on giving 1.75 ns pulses (FWHM) every 16.7 ns. Fast extraction without the flat-tops would provide 64 μA currents. Storage rings have not been included in the initial proposal, but space is available for later installation of collector and stretcher rings. This will enable the main ring cycle rate to be increased to 10 Hz and the average fast- or slow-extracted current to be increased to 96 μA.

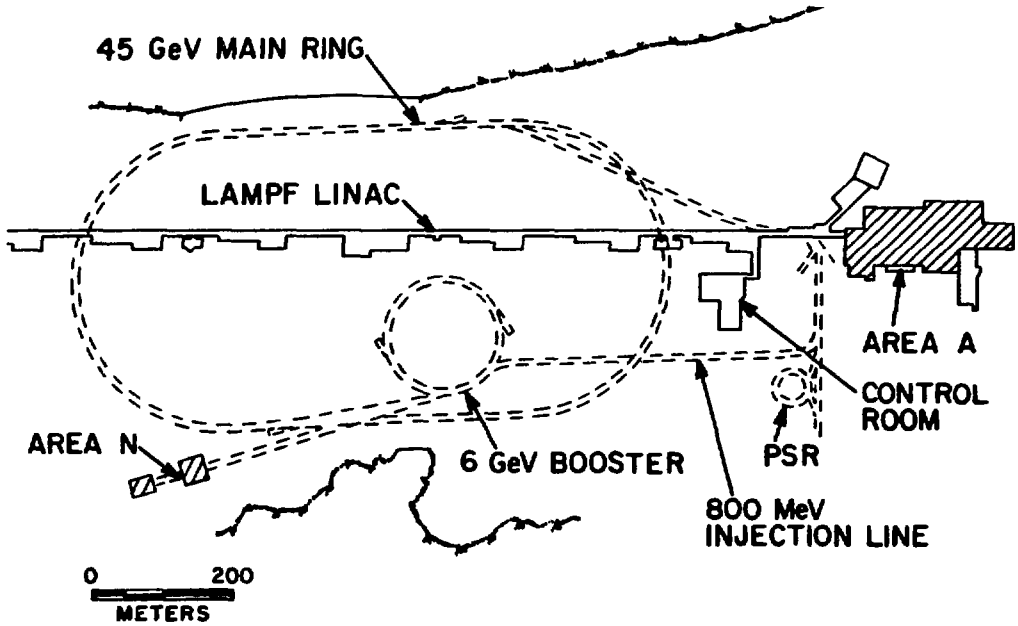

Figure 23: Site plan of the proposed LAMPF II accelerators and experimental areas.

In the latest design both synchrotrons use separated-function magnets. The booster lattice has a superperiodicity $S = 6$, created by omitting the dipoles from every other focusing cell and modulating the lengths of the cells. The choice of working point ($\nu_x = 5.22$, $\nu_y = 4.28$) drives transition above the top energy ($\gamma_t = 14.5$). The six short empty cells are then used to accommodate 18 rf cavities, while the long empty cells are available for beam transfer elements.

The main ring race-track lattice consists of several functionally different sections—two 144° bending arcs, four 18° missing magnet dispersion suppressors, four short matching sections, and two 90 m long straight sections to accommodate rf cavities, beam transfer elements, and Siberian snakes. The 28 m long high-β section will reduce the beam spill on the extraction septum. The working point ($\nu_x = 7.45$, $\nu_y = 6.45$) was chosen close to a half-integer resonance for slow extraction. The high average dispersion in the bending arcs ($\eta_x \simeq 6$m) keeps the transition energy below the acceleration range ($\gamma_t = 6.4$, 5.06 GeV).

The Los Alamos group is pioneering a number of potentially important technical developments. First among these is the use of an asymmetric magnet cycle (Praeg, 1983), (see above) with slow rise and fast fall to reduce the rf voltage requirements. In the latest design this scheme is applied only to the booster synchrotron. For the main ring a linear ramp is proposed with equal 50 ms rise and fall times. Instead of a resonant power supply system this would use SCR bridge rectifiers operating from three phase 60 Hz, supplied by a generator-flywheel set.

To achieve tunable high-power rf cavities economically, the Los Alamos group are proposing to bias the ferrite with magnetic field perpendicular to that of the rf, rather than parallel, as has been conventional. Figure 24 shows how with TDK G26 ferrite this results in cavities with much higher Q values. Tests of a full-scale cavity under high-power conditions are beginning in the laboratory, and will be continued in an existing machine such as the Los Alamos Proton Storage Ring under high beam-loading conditions.

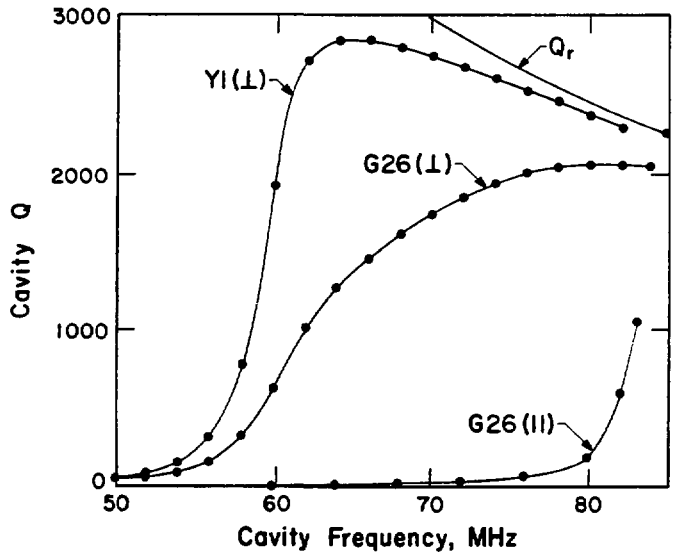

Figure 24: Frequency variation of the Q-factor of test cavities for perpendicular- and parallel-biassed ferrite.

The third development concerns the design of suitable vacuum chambers for the fast-cycling magnets. There must be a conducting surface on the inside of the chamber to prevent the build-up of electrostatic charge and also to provide a low-impedance path for the high-frequency image currents involved in maintaining beam stability. On the other hand eddy currents must be suppressed to minimize heating and magnetic field distortion.

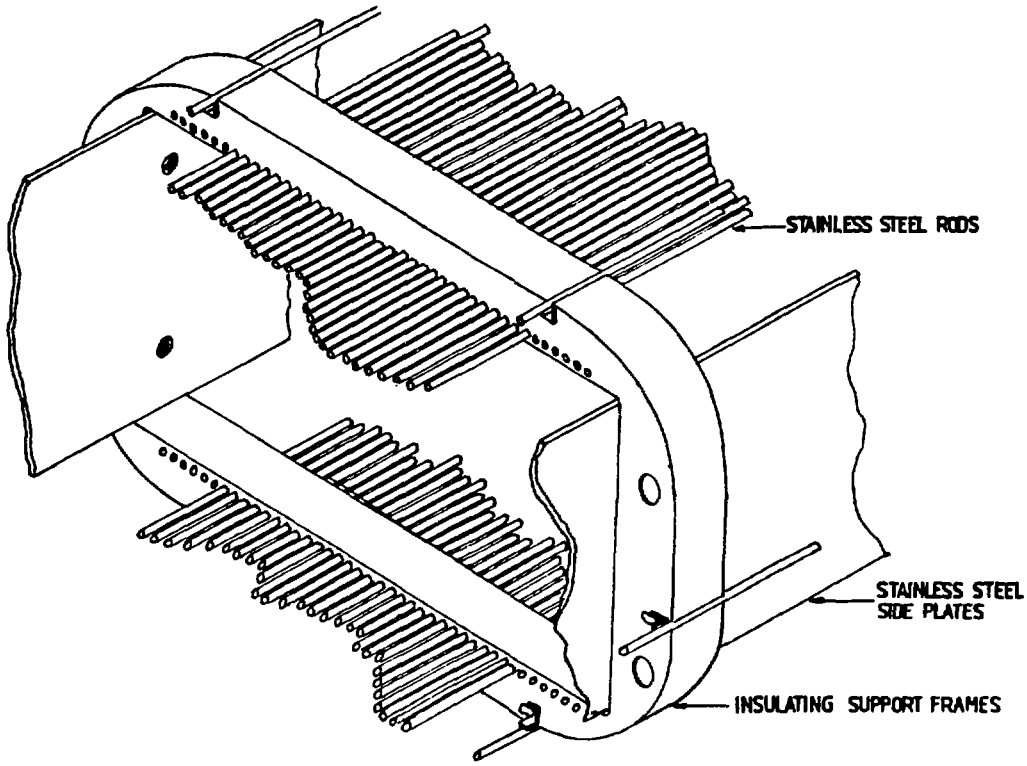

Figure 25: Ceramic vacuum chamber and wire rf shield used in the Rutherford ISIS synchrotron.

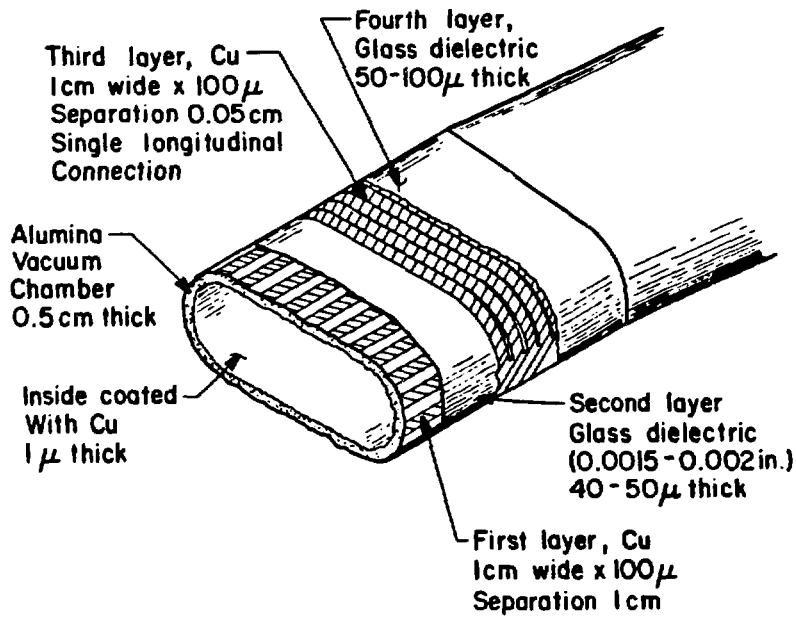

Figure 26: Los Alamos design for booster dipole magnet vacuum chamber.

The only present example of such a system is at the Rutherford ISIS synchrotron (Bennett and Elsey, 1981), where a ceramic vacuum chamber is used, fitted with an internal cage of longitudinal wires to provide an rf shield (Fig. 25). The Los Alamos group is building test sections of a ceramic vacuum chamber with the conducting surfaces provided by an internal 1 m copper coating and external layers of copper strips (Fig. 26). The system offers a smaller magnet aperture but will require careful design of the end connections.

The initial proposal appeared in December 1984, the second edition in May 1986. The cost has been reduced somewhat by eliminating one experimental area. This has been done without cutting down the number of secondary channels by using the MAXIM scheme of C. Tschalär (1986) to produce beams to the left and right of each target. The total cost, including ED&I but not contingency, is estimated to be M$328 (FY 1985 US dollars).

EUROPEAN HADRON FACILITY

The first European scheme for a kaon factory came from SIN. This was for a 20 GeV 80 μA synchrotron fed from the 590 MeV SIN cyclotron and the proposed ASTOR isochronous storage ring (Joho, 1984). Rapidly growing support led to the formation of an international study group. The conceptual design has been discussed at a number of workshops during the last nine months, and the reference design was agreed on in March (EHF Study Group, 1986).

The layout of the proposed EHF is shown in Fig. 27. To accelerate 100 μA to 30 GeV the main ring cycles at 12.5 Hz; it is fed by a 9 GeV booster of half the circumference

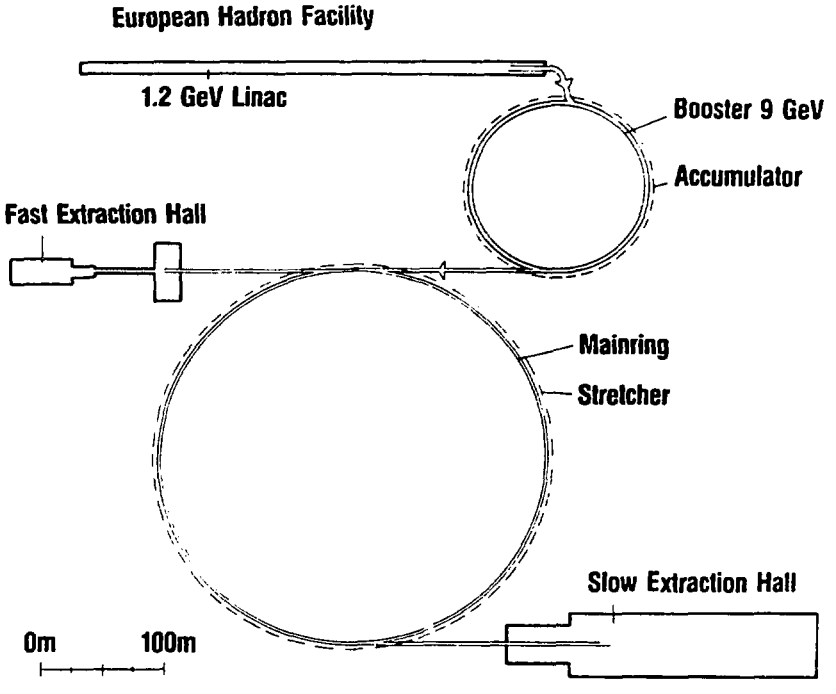

Figure 27: Schematic layout of the European Hadron Facility.

and a specially designed 1.2 GeV linac, both cycling at 25 Hz. Collector (here called "accumulator") and stretcher rings are included in the design to follow the booster and main ring, respectively. The choice of a relatively high 9 GeV for the booster energy raises the cost of the entire project by about 10% over the minimum at 4 GeV but offers a number of advantages. Not only does it provide greater opportunities for interesting physics at an intermediate construction stage but it brings the booster radius to half that of the main ring, allowing the collector to be placed in the booster tunnel, halving its length and equalizing the number of rings in each tunnel. The desire to accelerate polarized protons plays an important role in this design, and with 9 GeV injection Siberian snakes in the main ring will cause less closed orbit distortion.

Although the design is officially "siteless" the circumference of the main ring has been chosen equal to that of the CERN ISR for reference purposes. The advantages of tunnel-stuffing are clearly as obvious in Europe as they have been in the USA. Besides the tunnel, CERN's site offers other advantages—the existence of interim injectors, the availability of the West Hall after the experimental program has moved to LEP, and the infrastructure (even if only as a model for an independent EHF laboratory). The most obvious advantage to CERN would be the provision of a back-up PS. But these are mere speculations and at the moment it seems more likely that the EHF would be located elsewhere, say in Italy or at SIN.

All the rings use separated-function magnets and superperiodic lattices with transition energy outside of the acceleration range. The booster uses an interesting doublet lattice with $S = 6$ and nine cells in each superperiod. Dipole magnets are omitted from three cells, two of which can then be made dispersionless and therefore ideal for the location of rf cavities. The quadrupole doublets give low β-functions and high tunes ($\nu_x = 13.4$, $\nu_y = 10.2$); the transition energy $\gamma_t = 12.7$. The main ring has eight superperiods with seven regular FODO cells in each; dipoles are omitted in four of the half-cells, bringing the dispersion close to zero in three of them grouped together. These provide 25 m long straight sections, four of which are used for rf cavities, two for Siberian snakes and two for beam transfer.

The 1200 MeV linear injector consists of a series of linacs of different types (Fig. 28). Following the H^- ion source and dc acceleration to 30 keV, two RFQs operating at 50 MHz and 400 MHz take the beam to 200 keV and 2 MeV, respectively. A 400 MHz drift tube linac then accelerates the ions to 150 MeV and finally a 1200 MHz side-coupled linac to 1200 MeV. Figure 28 also illustrates the time structure, showing how only two out of 24 SCL buckets are filled. These are then painted over the central 50% of the 50 MHz booster bucket to provide the desired density distribution.

Work is continuing with the aim of producing a formal proposal within about a year. Some temporary office space has been made available at CERN and the study group plans to make this their headquarters. The total cost is estimated to be MDM867, not including controls, contingency or inflation.

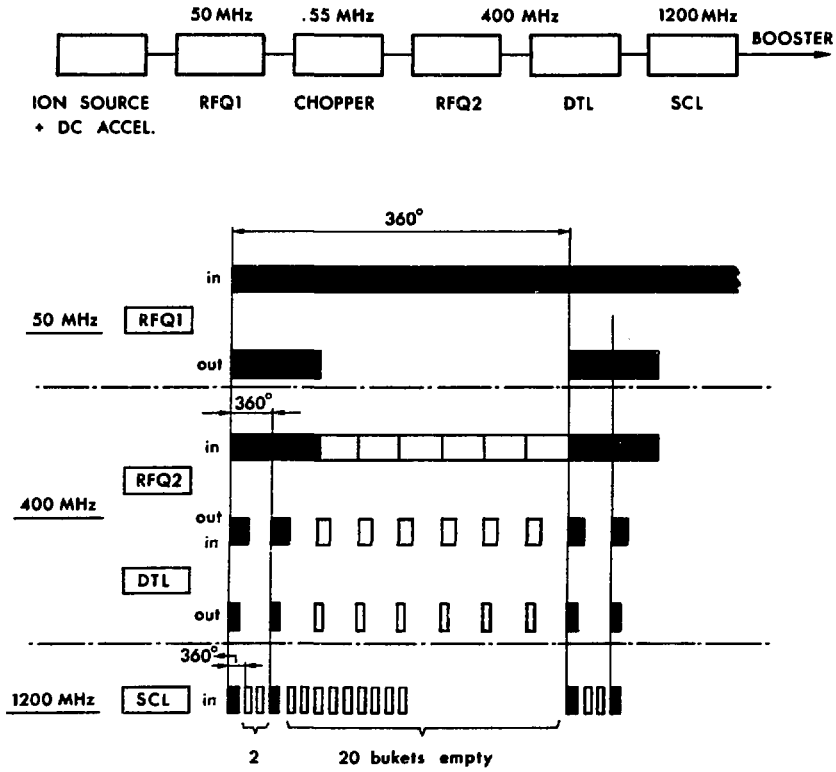

Figure 28: Schematic diagram of the E.H.F. linear accelerators and of the phase-compression of the dc beam from the ion source into the 2:8 bucket scheme for optimal injection into the Booster.

JAPANESE PROPOSALS

There is considerable interest in kaon factories in Japan, with schemes being promoted by Kyoto University and jointly by KEK and the University of Tokyo.

The most fully developed scheme is that from Kyoto, where for some time there has been a proposal for an 800 MeV linac pion factory. The proposed kaon factory complex (Imai *et al.*, 1984) would add an 800 MeV compressor ring, a 25 GeV fast-cycling synchrotron, a stretcher ring, and antiproton accumulation and storage rings. The linac would operate at 60 Hz, feeding every other pulse to the synchrotron, operating at 30 Hz with an average current of 50 μA. The magnet lattice has a superperiodicity $S = 4$ with regular FODO cells and dispersion-free straight sections. The betatron tunes are $\nu_x = 11.2$, $\nu_y = 10.2$; the transition $\gamma_t = 7.9$ GeV.

At KEK and the University of Tokyo there has been a longstanding interest (Yamazaki, 1985) in increasing the intensity of the KEK 12 GeV PS by using a higher energy booster (1–3 GeV). There is also the independent GEMINI project, (Sasaki *et al.*, 1984) a spallation neutron source and pulsed muon facility, based on an 800 MeV synchrotron operating at 50 Hz to produce 500 μA proton beams. There is now a move to combine these schemes into a single coherent project which might also act as the injector of a kaon factory. One scheme which is being considered would involve a 30 GeV, 30 μA proton synchrotron cycling at 1 Hz fed by a 3 GeV, 100 μA booster cycling at 15 Hz. The booster might be a new fast-cycling

synchrotron or it could be a combination of GEMINI with a 3 GeV FFAG after-burner. The booster would form the core of a multi-purpose laboratory, feeding not only the main ring but also a storage ring for spallation neutrons and pulsed muons. The acceleration of heavy ions is also being considered.

A meeting is expected to be held shortly by the proponents of all these schemes to settle the parameters of an accelerator complex—referred to as the "large hadron project"—satisfying their various needs. A possible arrangement of the booster stages is shown in Fig. 29. Here a heavy ion linac (8 MeV/nucleon) and a proton linac (1 GeV) are shown feeding individual booster and cooler rings; these in turn supply the existing 12 GeV synchrotron, or in a later phase, a new 30 GeV synchrotron.

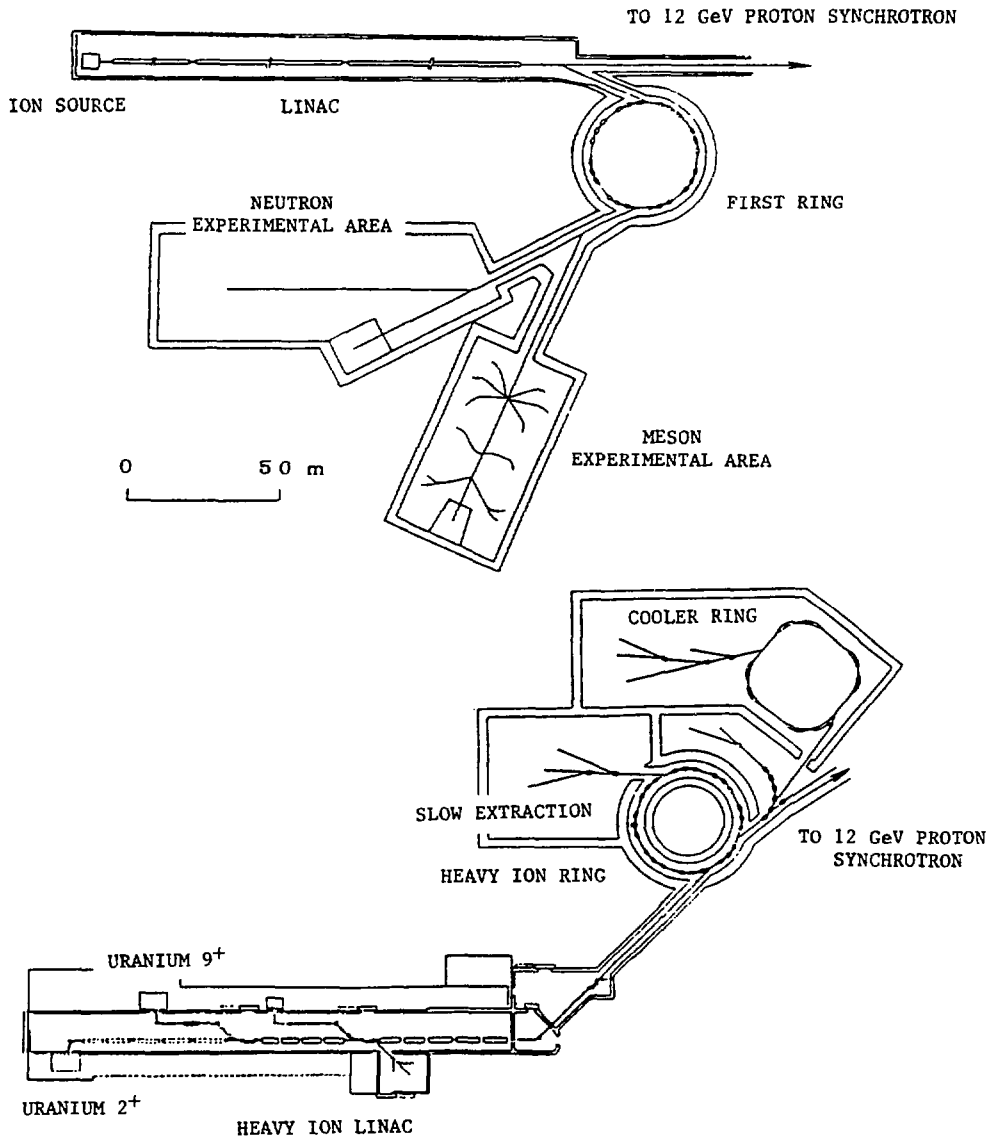

Figure 29: Booster accelerator complex for the Japanese Large Hadron Project.

CONCLUSIONS

There is active interest in a number of fields in building circular proton accelerators with the highest possible beam intensity. At low energies isotope production and cancer therapy provide the rationale for high current cyclotrons. At higher energies a variety of important questions in both particle and nuclear physics could be attacked using the more intense and/or clean beams of kaons, antiprotons, neutrinos and other particles that high-intensity proton synchrotrons could supply. In response to these rich possibilities a booster is under construction at the Brookhaven AGS and proposals for kaon factories have been completed at LAMPF and TRIUMF and are in preparation in Europe and Japan. The concept of beam brightness has played a major role in determining the number of stages in these machines and in the Superconducting Super Collider.

ACKNOWLEDGEMENTS

The author is delighted to acknowledge the information and material that have been generously supplied to him by Drs. F. Bradamante, M. Inoue, T. Ludlam, A. Masaike, H. Sasaki, T. Suzuki, H.A. Thiessen, and T. Yamazaki. He has been heavily dependent on previous authors covering this ground and hopes that imitation of their treatments will be treated as flattery rather than plagiarism. He is also very grateful for the comments of colleagues at TRIUMF on the manuscript, especially to Richard Baartman. Finally it is a pleasure to acknowledge Denise Dale's and Lorraine King's meticulous typing, Anna Gelbart's and Terry Bowyer's excellent drawings and Fred Jones' and Alistair Martin's impressive computer graphics.

REFERENCES

Ankenbrandt, C., 1984
The case for a small SSC booster, *Proc. 1984 Summer Study on the Design and Utilization of the Superconducting Super Collider, Snowmass*, ed. R. Donaldson, J.G. Morfin, (Division of Particles and Fields of the American Physical Society), p. 315.

Bennett, J.R.J., and Elsey, R.J., 1981
Glass-jointed alumina vacuum chambers, *IEEE Trans. Nucl. Sci.*, **NS-28**:3336.

Botman, J.I.M., Craddock, M.K., Kost, C.J. and Richardson, J.R., 1983
Magnet sector design for a 15 GeV superconducting cyclotron, *IEEE Trans. Nucl. Sci.*, **NS-30**:2007.

Boussard, D., 1975
Observation of microwave longitudinal instabilities in the CPS, CERN-Lab:II/RF/Int./75–2.

Bovet, C., Gouiran, R., Gumowski, I, and Reich, K.H., 1970
A selection of formulae and data useful for the design of A.G. synchrotrons, CERN/MPS-SI/Int. DL/70/4.

Bradamante, F., 1986
Conceptual design of the EHF, INFN/AE-86/7.

Brookhaven National Laboratory, 1984
AGS booster conceptual design report, BNL-34989.

Bruck, H., 1966
Accélérateurs Circulaires de Particules, Presses Universitaires, Paris. [Available in an English translation as Los Alamos report LA-TR-72-10].

CERN — International School on Particle Accelerators, 1977
Theoretical aspects of the behaviour of beams in accelerators and storage rings, Erice, 1977, ed. M.H. Blewett, CERN 77-13.

CERN Accelerator School, 1985
General accelerator physics, ed. P. Bryant and S. Turner, CERN 85-19.

Courant, E.D., Livingston, M.S., and Snyder, H.S., 1952
The strong focusing synchrotron—a new high energy accelerator, *Phys. Rev.*, **88**:1190.

Courant, E.D., 1968
Accelerators for high intensities and high energies, *Ann. Rev. Nucl. Sci.*, **18**:435.

Courant, E.D., 1986
Private communication.

EHF Study Group, 1986
Feasibility study for a European Hadron Facility, ed. F. Bradamante, J. Crawford and P. Blüm, EHF-86-33.

Hofmann, A., and Pedersen, F., 1979
Bunches with local elliptic energy distributions, *IEEE Trans. Nucl. Sci.*, **NS-26**:3526.

Imai, K., Masaike, A., Matsuki, S., and Takekoshi, H., 1984.
A proposal of high intensity accelerator complex for meson science in Kyoto University, *Proc. 5th Symposium on Accelerator Science and Technology, KEK*, p. 396.

Joho, W., 1974
Application of the phase compression – phase expansion effect for isochronous storage rings, *Part. Accel.*, **6**:41.

Joho, W., 1984
Interfacing the SIN ring cyclotron to a rapid cycling synchrotron with an Acceleration and STOrage Ring ASTOR, *Proc. 10th. Int. Conf. on Cyclotrons and their Applications*, East Lansing, ed. F. Marti, IEEE, New York, p. 611.

Joho, W., Adam, S., Berkes, B., Blumer, T., Humbel, M. Irminger, G., Lanz, P., Markovits, C., Mezger, A., Olivo, M., Rezzonico, L., Schryber, U., and Sigg, P., 1985
Commissioning of the new high intensity 72 MeV injector II for the SIN ring cyclotron, *IEEE Trans. Nucl. Sci.*, **NS-32**:2666.

Keil, E., and Schnell, W., 1969
Concerning longitudinal stability in the ISR, CERN-ISR-TH-RF/69–48.

Kelly, E.L., Pyle, R.V., Thornton, R.L., Richardson, J.R., and Wright, B.T., 1956
Two electron models of a constant frequency relativistic cyclotron, *Rev. Sci. Instr.*, **27**:493.

Khoe, T.K., and Kustom, R.L., 1983
ASPUN, Design for an Argonne Super intense PUlsed Neutron source, *IEEE Trans. Nucl. Sci.*, **NS-30**:2086.

Laclare, J.-L., 1986
Beam current limits in circular accelerators and storage ring longitudinal coasting beam instabilities, *Proc. NATO ASI Course on High Brightness Accelerators*, Pitlochry, 1986 (to be published).

Laslett, J.L., 1963
On intensity limitations imposed by transverse space-charge effects in circular particle accelerators, *Proc. Brookhaven Summer Study on Storage Rings*, BNL-7534, p. 324.

Lawrence, E.O., and Edlefsen, N.F., 1930
On the production of high speed protons, *Science*, **72**:376.

Lee, Y.Y., 1985
The AGS improvement program, *IEEE Trans. Nucl. Sci.*, **NS-30**:1607.

Livingood, J.J., 1961
Cyclic Particle Accelerators, van Nostrand, Princeton.

Livingston, M.S. and Blewett, J.P., 1962
Particle Accelerators, McGraw-Hill, New York.

Los Alamos National Laboratory, 1984
A proposal to extend the intensity frontier of nuclear and particle physics to 45 GeV (LAMPF II), LA-UR-84-3982.

Los Alamos National Laboratory, 1986
The physics and a plan for a 45 GeV facility that extends the high-intensity capability in nuclear and particle physics, LA-10720-MS.

McMillan, E.M., 1945
The synchrotron—a proposed high energy accelerator, *Phys. Rev.*, **68**:143.

Meads Jr., P.F., and Wüstefeld, G., 1985
An FFAG compressor and accelerator ring studied for the German spallation neutron source, *IEEE Trans. Nucl. Sci.*, **NS-32**:2697.

Praeg, W.F., 1983
Dual frequency ring magnet power supply with flat-bottom, *IEEE Trans. Nucl. Sci.*, **NS-30**:2873.

Reich, K.H., Schindl, K., and Schönauer, H., 1983
An approach to the design of space charge limited high intensity synchrotrons, *Proc. 12th Int. Conf. on High Energy Accelerators*, ed. F.T. Cole, R. Donaldson, Fermilab, p. 438.

Richardson, J.R., MacKenzie, K.R., Lofgren, E.J., and Wright, B.T., 1946
Frequency modulated cyclotron, *Phys. Rev.*, **69**:669.

Richardson, J.R., 1965
Sector focusing cyclotrons, *Prog. Nucl. Techniques & Instrumentation*, **1**:1.

Sasaki, H., and GEMINI Study Group, 1984
Accelerator project GEMINI for intense pulsed neutron and meson source at KEK, *Proc. Int. Collaboration on Advanced Neutron Sources VII*, Chalk River, September 1983, AECL-8488, p.50.

Symon, K.R., Kerst, D.W., Jones, L.W., Laslett, L.J., and Terwilliger, K.M., 1956
Fixed field alternating gradient particle accelerators, *Phys. Rev.*, **103**:1837.

Thomas, L.H., 1938
The paths of ions in the cyclotron, *Phys. Rev.*, **54**:580.

TRIUMF, 1985
KAON factory proposal, TRIUMF, Vancouver.

Tschalär, C., (in press)
Multiple achromatic extraction system, *Nucl. Instrum. Methods.* (in press)

U.S. Summer Schools on High Energy Particle Accelerators, 1981–
Physics of high energy particle accelerators, *A.I.P. Conf. Proc.*, vols. **87, 92, 105, 127, 153.**

Veksler, V.I., 1944
A new method for acceleration of relativistic particles, *Doklady*, **43**:329; *J. Physics USSR*, **9**:153.

Wienands, U., and Craddock, M.K., 1986
Variation of cost of KAON factory accelerators with beam energy and intensity, TRIUMF internal report TRI-DN-86-7.

Wilson, E.J.N., 1977
Proton synchrotron accelerator theory, CERN 77-07.

Yamazaki, T., 1985
Toward high intensity proton facilities—a promising future of the KEK accelerator complex, *Proc. KEK Workshop on Future Plans for High Energy Physics*, preprint UTMSL-116.

Zach, M., Dutto, G., Laxdal, R.E., Mackenzie, G.H., Richardson, J.R., Trellé, R., and Worsham, R., 1985
The H^- high intensity beam extraction system at TRIUMF, *IEEE Trans. Nucl. Sci.*, **NS-32**:3042.